

NEAR-SURFACE CO₂ TUNABLE DIODE LASER ABSORPTION SPECTROSCOPY
CONCENTRATION MEASUREMENTS IN THE LENS-XX EXPANSION TUNNEL
FACILITY

by

Joshua Michael Weisberger

February 5, 2015

A thesis submitted to the
Faculty of the Graduate School of
the University at Buffalo, State University of New York
in partial fulfillment of the requirements for the
degree of

Master of Science

Department of Mechanical and Aerospace Engineering

UMI Number: 1594791

All rights reserved

INFORMATION TO ALL USERS

The quality of this reproduction is dependent upon the quality of the copy submitted.

In the unlikely event that the author did not send a complete manuscript and there are missing pages, these will be noted. Also, if material had to be removed, a note will indicate the deletion.



UMI 1594791

Published by ProQuest LLC (2015). Copyright in the Dissertation held by the Author.

Microform Edition © ProQuest LLC.

All rights reserved. This work is protected against unauthorized copying under Title 17, United States Code



ProQuest LLC.
789 East Eisenhower Parkway
P.O. Box 1346
Ann Arbor, MI 48106 - 1346

Acknowledgments

I would first like to thank my advisor, Dr. Paul E. DesJardin, for his support, enlightening discussions, and guidance throughout this process. I would like to thank Dr. Matthew MacLean for his endless knowledge of the CUBRC facilities and computational efforts, and Dr. Ron Parker for his expertise and help in the experimental setup of the laser diagnostics. Thank you to my committee members, Dr. James Felske and Dr. Jon Yoo, for questions and conversations that improved that quality of this work. Thank you to Dr. Zakery Carr for being there to help whenever I had a question about the experimental setup. I am deeply appreciative of Gary Paone at CUBRC for always being there to lend a hand when two would not suffice. Without the support of everyone at CUBRC, this work would not have been possible; thank you for making me feel right at home. Thanks to everyone in the CET lab for providing useful input and a different way of looking at things. Finally, I would like to thank my family. While you may not always understand what I do, your interest and support in my endeavors makes everything worthwhile.

This work was sponsored by the Air Force Office of Scientific Research under the Multidisciplinary University Research Initiative entitled Fundamental Processes in High-Temperature Hypersonic Flows, Prime Award FA9550-10-1-0563. The views and conclusions contained herein are those of the authors and should not be interpreted as necessarily representing the official policies or endorsements, either expressed or implied, of the AFOSR or the U.S. Government.

Table of Contents

Acknowledgments	ii
List of Figures.....	iv
Nomenclature.....	vi
Abstract.....	viii
1 Introduction.....	1
2 Experiments.....	4
2.1 LENS-XX Facility and Experimental Setup.....	4
2.2 Line Selection for TDLAS.....	6
2.3 Diagnostic Measurement Setup.....	7
3 Modeling and Data Analysis.....	14
3.1 Computational Fluid Dynamics.....	14
3.2 Line-by-Line Model.....	17
3.3 Raw Data Analysis.....	19
4 Results and Discussion.....	27
4.1 CFD and LBL Modeling.....	27
4.2 Sensitivity Studies.....	28
4.3 Data and Simulation Comparison Results.....	32
5 Conclusion.....	50
Bibliography.....	52

List of Figures

Fig. 1	Aluminum cylinder installed in the LENS-XX expansion tunnel	10
Fig. 2	Time varying pitot pressure during the entire run. Ramp 1 and 2 time durations are shown as red lines	11
Fig. 3	Transmission plot from simulation of normal run CO ₂ levels and nominal laboratory conditions for H ₂ O experienced during a run	12
Fig. 4	Top view schematic of experimental optical bench setup	13
Fig. 5	Portion of raw data from run, with ramps 1 and 2 highlighted in red	22
Fig. 6	Transformation of single raw data ramp to transmission data	23
Fig. 7	Background (red) and baseline (blue) used to transform raw data to transmission data	24
Fig. 8	Example wavenumber calibration showing raw data along with HITRAN simulation fit	25
Fig. 9	Pre-run full-width half-maximums of wavenumber calibration	26
Fig. 10	Normalized temperature, normalized pressure, and mole fraction freestream profiles for half the width of the expansion tube. The two insets show detail of the contour shape for both normalized pressure and mole fraction of CO ₂	34
Fig. 11	Schematic of top view of cylinder flow cut along stagnation line with appropriate regions labeled, including freestream, expanding flow, and surface flows	35
Fig. 12	Shock layer profiles for temperature, pressure, and mole fraction for both the (a) non-catalytic and (b) super-catalytic cases	36
Fig. 13	Flowchart for the line-by-line transmission spectrum simulation code	37
Fig. 14	Schematic for sensitivity studies showing stagnation line angle, element width, and element distance off the surface of the cylinder. The inset shows a schematic for the number of simulated points on the detector element	38
Fig. 15	Transmission plots for various number of polyline points extracted from the CFD results	39

Fig. 16	Screw and hollow tube placed adjacent to cylinder for magnification measurement	40
Fig. 17	Pixel size transmission comparisons for (a) non-catalytic cases and (b) super-catalytic cases	41
Fig. 18	Distance off cylinder surface comparisons for (a) non-catalytic cases and (b) super-catalytic cases	42
Fig. 19	Angle of pixel element off the stagnation line comparison for (a) non-catalytic cases and (b) super-catalytic cases	43
Fig. 20	Transmission plots for full pixel simulation (20x5) and single line pixel simulation (20x1) for the (a) non-catalytic case and (b) super-catalytic cases	44
Fig. 21	Stagnation line mole fraction profiles in (a) the shock layer for various reaction efficiencies, with (b) zoom-in view of near-surface region	45
Fig. 22	Temperature dependence of CO ₂ transition used in experiment	46
Fig. 23	RMS error of the residual between raw data and simulations for both ramps 1 and 2	47
Fig. 24	Experimental results and simulations for non-catalytic, super-catalytic, and reaction efficiency $\gamma = 0.00025$ for ramp 1 shown in (a). A zoomed in view of the absorption feature is shown in (b), with the residual in (c) for $\gamma = 0.00025$	48
Fig. 25	Experimental results and simulations for non-catalytic, super-catalytic, and reaction efficiency $\gamma = 0.0005$ for ramp 2 shown in (a). A zoomed in view of the absorption feature is shown in (b), with the residual in (c) for $\gamma = 0.0005$	49

Nomenclature

E''	Transition lower-state energy, [cm^{-1}]
hc/k	Second radiation constant, [$cm \cdot K$]
I	Transmitted intensity
I_o	Incident intensity
k_ν	Spectral absorption coefficient, [cm^{-1}]
$k_\nu L$	Absorbance
L	Optical path length, [cm]
M	Molecular weight of absorbing molecule, [g/mol]
n	Collisional broadening exponent
P	Total pressure, [atm]
Q	Partition function
$S_i(T)$	Temperature dependent transition linestrength, [$cm^{-2} \cdot atm^{-1}$]
T	Temperature, [K]
\dot{w}	Molar production rate, [$mol \cdot m^{-2} \cdot s^{-1}$]
X	Absorbing species mole fraction
Y	Absorbing species mass fraction
$\Delta\nu_C$	Collisional full width at half maximum, [cm^{-1}]
$\Delta\nu_D$	Doppler full width at half maximum, [cm^{-1}]
γ	Catalytic recombination parameter
δ_{air}	Air-broadening half-width, [$cm^{-1} \cdot atm^{-1}$]

δ_{self}	Self-broadening half-width, [$cm^{-1}\cdot atm^{-1}$]
ν_o	Linecenter wavenumber, [cm^{-1}]
φ_ν	Transition lineshape function, [cm]
Γ	CO impingement flux, [$mol\cdot m^{-2}\cdot s^{-1}$]

Abstract

Measurements of carbon dioxide concentration are made in the LENS-XX expansion tunnel facility at CUBRC to investigate the effects of surface catalysis on vehicles in hypersonic flows. A high-resolution tunable diode laser absorption spectroscopy setup probes the P36e carbon dioxide absorption line of the $\nu_1 + \nu_3$ combination band located at $2.7153 \mu\text{m}$ (3682.765 cm^{-1}). Numerical simulations are computed with DPLR using the specified reaction efficiency surface catalysis model. Absorption measurements adjacent to the surface of a 2 inch diameter, 2.5 inch long aluminum cylinder correlate well with simulations indicating only small amounts of catalytic behavior at the surface. The velocity, density, freestream temperature, specific enthalpy, and stagnation point pitot pressure of the run are 4.6 km/s ($M = 7.1$), 1.53 g/m^3 , 1328.4 K , 11.75 MJ/kg , and 31.6 kPa , respectively. The simulation of the absorption spectrum is performed using a non-homogeneous line-by-line code utilizing the HITRAN database for spectroscopic parameters. Input data for the line-by-line code is obtained from computational fluid dynamics simulations of both the cylinder and the expansion tunnel facility. Specified reaction efficiency for the mechanism $\text{CO} + \text{O} \rightarrow \text{CO}_2$ is determined inversely using detailed CFD and comparisons to experimental measurements. The catalysis model specifies a reaction-specific efficiency that determines the fraction of reactants reaching the surface for which a recombination event occurs. Best agreement was found for $\gamma_{\text{CO}} = 0.00025$ to 0.0005 , indicating that the coupled line-by-line code and CFD approach is useful for assessing near-surface composition using tunable diode laser absorption measurements of hypersonic flows.

1 Introduction

Mars has become the primary focus for planetary exploration missions. When entering its atmosphere at hypersonic speeds, a shock wave develops in front of the vehicle. The kinetic energy associated with flight at these speeds results in extremely high temperatures behind the shock. In order to retain the structural integrity of the vehicle, a thermal protection system (TPS) is often used to protect against the harsh environment. High speed entry is a critical design consideration, and the design of an adequate TPS is crucial for decreasing the weight of the vehicles and cost of the launches. Aerothermal heating includes contributions from radiation, convection, and air/surface chemistry. An important source of chemical heating is the catalytic exothermic recombination of atoms and molecules on the TPS surface. Often, the TPS is over-designed by using the most conservative estimate for heat flux, which corresponds to the super-catalytic boundary condition. Using a more accurate surface catalysis model can allow for more efficient designs of the TPS for a given vehicle and mission.

The Martian atmosphere is made up of approximately 95.7% CO_2 with other trace species. Catalytic heating does occur for Earth reentry, but is more pronounced in the carbon dioxide environments of Mars. This is in part due to the large exothermic recombination reaction of CO and O forming CO_2 [1]. Recombination at or near the surface of species dissociated in the shock layer leads to higher levels of heating at the vehicle surface due to the energy released from the recombination process. At higher speeds, the effects of catalysis become increasingly important when calculating heat loads on the surface [2]. Uncertainty in catalytic behavior of the surface is a challenge when trying to find heating rates and transition onset criteria [3]. The main problem

that catalysis poses is that in order to understand ground test measurements and validate computational fluid dynamics (CFD) using those measurements, the surface catalysis of the particular model tested must be known and an extrapolation is necessary to both the environment and the TPS material of the flight vehicle. However, catalytic mechanisms are not fully understood.

Certain mechanisms have been postulated to be present, including the Langmuir-Hinshelwood (L-H) and Eley-Rideal (E-R) mechanisms. The L-H mechanism describes the interaction between two adsorbed molecules, while the E-R mechanisms describe the interaction between an adsorbed molecule and a gas phase molecule. Catalytic surface modeling has been taken into account in recent CFD codes. There are multiple methods of including catalytic wall boundary conditions, some more physical than others. The non-catalytic and super-catalytic surface boundary conditions provide a lower and upper bound on surface heating, respectively. In the super catalytic case, the gas mixture is returned to its lowest chemical energy state at the wall, releasing the energy back into other modes in the flow. For cold wall ground test environments in a pure CO₂ test gas, this corresponds to the CO₂ returning back to its freestream mass fraction of unity. This boundary condition is non-physical because it does not include rate limitation or reactant availability in describing how the recombination has occurred. A specified reaction efficiency (SRE) model has been used in which a catalytic recombination efficiency is specified that relates the number of reactants that recombine at the surface to the total number that reach the surface. The SRE model is more physical in that it accounts for reactant and product availability through species mass balance at the surface, but the reaction efficiency, γ , must be known for each reaction and specifying significant numbers of reactions in which reactants are consumed by multiple pathways can be very complex. Quantification of individual reaction pathways that provide the most

significant energetic changes to gas composition is therefore critical in implementing a relevant surface catalysis model.

Clearly, state-of-the-art hypersonic flow modeling suffers from unknown properties near the vehicle surface. The objective of this study is to provide some of this missing information using tunable diode laser absorption spectroscopy (TDLAS) measurements. TDLAS has been around since the early 80s, and measurement capabilities continue to improve rapidly with advancing technology in the fields of diode laser, optics, and detectors. Recent reviews on the use of TDLAS can be found in [4] for application to low-speed reacting flows. Significant additional challenges are also introduced with the application to high-speed flows. Due to the very short test times, the laser must tune extremely fast and the signal to noise is challenging because multiple absorption sweeps are often not possible. TDLAS experiments have been successfully performed in NO [5-9], H₂O [10-12], CO [11, 13], and CO₂ [14-17] environments. A TDLAS system used for monitoring CO₂ at 2.7 μm was constructed and tested in both a free piston tunnel (VKI Longshot) and an arc jet tunnel (ONERA F4) [18]. This study represents the first use of TDLAS measuring CO₂ at a wavelength of 2.753 μm (3682.765 cm^{-1}) in a high-speed expansion tunnel where CO₂ absorption measurements are made in the near-field flow of an aluminum cylinder. These measurements are compared to numerical modeling predictions using line-by-line (LBL) calculations coupled with CFD predictions.

The rest of this study is organized as follows. Section 2 describes the experimental setup using the CUBRC LENS-XX facility and TDLAS measurements. Section 3 details the LBL and CFD modeling employed for comparison to measurements. Sections 4 and 5 summarize the processing of the raw TDLAS data and presents the results showing comparisons of model predictions to data. Finally, Section 6 concludes.

2 Experiments

2.1 LENS-XX Facility and Experimental Setup

The Calspan University at Buffalo Research Center (CUBRC) currently operates a 48” shock tunnel, the LENS-I and LENS-II reflected shock tunnels, and the LENS-XX expansion tunnel. These tunnels are used for aero-thermal and aero-optic testing and evaluation of flight vehicles. In this study, measurements are conducted in LENS-XX. The appeal of using this facility is that the maximum temperature of the gas prior to interaction with the test article is significantly lower than from a reflected shock tube or arc jet facility, thereby more closely matching reentry flight conditions and minimizing freestream contamination from gas dissociation.

Peak temperatures in the reflected shock tunnels are extremely high because the energy is added through a strong shock that stagnates the test gas. This leads to dissociation of the test gas that affects the chemical composition of the freestream flow. In an expansion tunnel, the majority of the energy is added to the flow through an unsteady expansion process. This results in a test gas that is free of dissociated species. This allows measurements to be made in conditions that more accurately mimic the flight of hypervelocity vehicles, and is especially important when characterizing surface catalysis. Further details of the facility can be found by Dufrene, *et al.* [19, 20]

In this study, the experiment consists of a cylindrical model composed of aluminum 2 *inches* (5.08 *cm*) in diameter and 2.5 *inches* (6.35 *cm*) in span and supported in the facility by rods from the aft (back) side of the cylinder as seen in Fig. 1. The cylinder is turned on a lathe prior to installation in the facility to ensure a smooth surface. The cylinder is exposed to air before the

test, and the usual oxide layer forms on the surface. The test section width is 2 feet, and is located in the expansion tube section of the facility. This allows for simpler interpretation of the results because the free jet shear layer that accompanies expansion into the 8-foot test section need not be included. The test condition in the facility is monitored by a Pitot probe mounted a few inches above the cylinder and placed in line with the front edge of the cylinder surface, which signals the arrival of the test gas and the duration of steady flow, which lasts about 400 microseconds for this particular condition. A plot of the time-varying pitot pressure can be seen in Fig. 2. The test gas for this flow condition is composed of a partial pressure of 25% CO₂ and 75% air. This composition is selected for two reasons. The first is to maximize sensitivity of the absorption feature without fear of oversaturation. There has been data presented in the literature supporting both the super-catalytic and near non-catalytic nature of the wall. Using preliminary CFD simulations with predicted characteristic parameters of the flow, a typical laser line-of-sight simulation was used to anticipate the absorption spectrum for the two catalytic extremes. The selected absorption line and freestream composition allowed for adequate absorption should the flow be non-catalytic, while remaining well below the saturation level should the flow be fully catalytic. The second is to produce a test condition with elemental composition similar to that produced by equilibrium ablation of a carbon ablator. The short-term goal of the experiment is to obtain cold-wall catalytic production data for CO₂, while the long-term goal of the effort is to employ the diagnostic and reduction technique for hot-wall (flight-relevant) production of carbon species by catalytic and oxidation processes.

The freestream condition for this run is as follows: $P = 516 \text{ Pa}$, $T = 1328.4 \text{ K}$, $\rho = 0.00153 \text{ kg/m}^3$, $U = 4603 \text{ m/s}$, $Y_{CO_2} = 0.337$, $Y_{N_2} = 0.507$, and $Y_{O_2} = 0.156$. The freestream enthalpy is 11.75 MJ/kg . All thermal degrees of freedom can be considered in

equilibrium with translation. The surface temperature of the cylinder remains fixed at its initial value of 300 K due to the short run time. The Pitot pressure at the stagnation point of the cylinder is 31.6 kPa . For this test case, the presence of CO_2 in the freestream complicates the line-of-sight integration of the absorption measurement, but because the pressure is significantly lower, the shape of the absorption signal is very different than that obtained for the surface. Therefore, it is straight forward to differentiate the two effects.

2.2 Line Selection for TDLAS

The selection of a molecular transition to probe depends on factors such as cost of the laser, availability of materials, interference of other spectral lines, sufficient absorption through the anticipated medium without saturation, and the scan range of the laser. A set of guidelines for selecting an absorption transition has been published by Zhou et al [21]. The particular CO_2 line in this study is selected because a conveniently packaged laser was available, other transitions do not interfere with the measurement, and sensitivity to pressure, temperature, and concentration changes is high. This laser is also well suited for freestream velocity measurements in the facility for a wide range of test conditions. The final selection is a laser that is capable of scanning the wavenumber region between approximately 3682.5 cm^{-1} and 3683 cm^{-1} .

It is necessary to ensure that the absorption lines from the water vapor in the laboratory air do not interfere with the measurement because the laser will pass through air on either side of the facility windows. The simulated spectra of both CO_2 and H_2O in the wavenumber scan range of the laser can be seen in Fig. 3. The parameters used for the H_2O simulation are based on normal conditions in the laboratory, and take into account the distance the laser travels through the air in the experimental setup; the path length is 60 cm , the temperature is 300 K , the pressure is 1 atm , and the mole fraction is 0.01 . The contribution from the water in the lab atmosphere over the

measured path length is nearly undetectable, indicating that this CO₂ line is a reasonable choice for these specific measurements.

2.3 Diagnostic Measurement Setup

The TDLAS setup operates as a pitch/catch system that spans the LENS-XX test section perpendicular to the flow direction. A schematic of the optical bench setup is shown in Fig. 4. The infrared (IR) laser light source is modulated from the pitch side of the tunnel, while the detector and acquisition system are operated from the catch side. The 0.635 *cm* diameter beam leaving the laser housing is collimated and turned 90 degrees through the use of a periscope assembly (Thorlabs, Inc.) to pass through the tunnel. The periscope allows lateral and multiple angular degrees of freedom when aligning the laser along the cylinder surface. The laser enters and exits the tunnel through two 1.75 *inch* diameter (clear aperture) CaF₂ windows with 30 minutes of wedge to reduce etaloning. CaF₂ windows are used for the tunnel windows due to their high transmission in the IR region, as well as their low index of refraction which allows them to be used without an anti-reflective coating. Beam steering from the wedge is taken into account during the alignment process. The size of the smallest aperture in the system ensures that the measurement is diffraction limited. From the pitch side of the optical setup, the collimated laser source is carefully aligned to follow the cylinder surface as it traverses the tunnel. In this arrangement, a ray from the laser source samples gas at a distance from the surface that remains constant over the cylinder length. After exiting the tunnel and passing through an achromatic imaging lens optimized for mid-IR wavelengths, the beam is split in two. Half the light is sent to the detector, while the other half is imaged onto a 640 x 512 pixel array IR camera to provide real-time images to check the alignment and verify the magnification.

The distributed feedback quantum cascade laser (NanoPlus GmbH) used in the experiment provides a scanning wavenumber range from 3682.5 cm^{-1} to 3683.0 cm^{-1} . A narrower tuning range between approximately 3682.71 cm^{-1} to 3682.81 cm^{-1} is used during the test to scan more slowly through the feature, avoiding lineshape smearing and increasing the number of data points describing the absorption feature. The beam is rapidly modulated to scan over this range by varying the temperature and injection current. The wavelength can be coarsely tuned by adjusting the temperature via the thermoelectric device to which the diode is mounted. For fine tuning capabilities, an ILX Lightwave LDC-3724C Laser Diode Controller regulates the temperature and current input to the laser, and receives as input a modified sawtooth waveform from a Tektronix AFG3102 arbitrary waveform generator. The LN_2 cooled InSb 32-element linear array IR detector (L-3 Cincinnati Electronics model SDD-2000-32-H) is coupled to a data acquisition system to acquire and store the signal at a frequency of 100 MHz .

The laser has an emission linewidth of less than 3 MHz (0.0001 cm^{-1}). At a scanning frequency of up to 6 kHz , this resolution has been shown to have a minimal effect on the measured absorption feature lineshape and can be neglected. At high modulation rates, the ideal linear ramp starts to become non-linear. Based on experience, the realistic maximum frequency for operation in a linear range is about 5 kHz . At this frequency, there will be four ramps per ms . For each ramp, the feature should have a sufficient amount of data points to accurately describe its shape, amplitude, and position. With a bandwidth of 100 MHz , 25,000 samples are acquired per ramp. This amount is more than sufficient to accurately capture the lineshape of the absorption feature. The temperature controller is set to $25\text{ }^\circ\text{C}$, and the modulation of the ramp amplitude is 0.56 V . The current is set to 140 mA , and the frequency of the waveform is 5 kHz .

While expansion tunnels can cause significant amounts of mechanical vibration, there is no movement of the facility until after the data is collected. This is verified using multiple channels on the linear array detector. When initially setting up the experiment, some of the pixels are shadowed by the cylinder surface. Movement of the shadow of the cylinder in the recorded data of the individual pixel elements occurs only after the test time is over.



Fig. 1: Aluminum cylinder installed in the LENS-XX expansion tunnel.

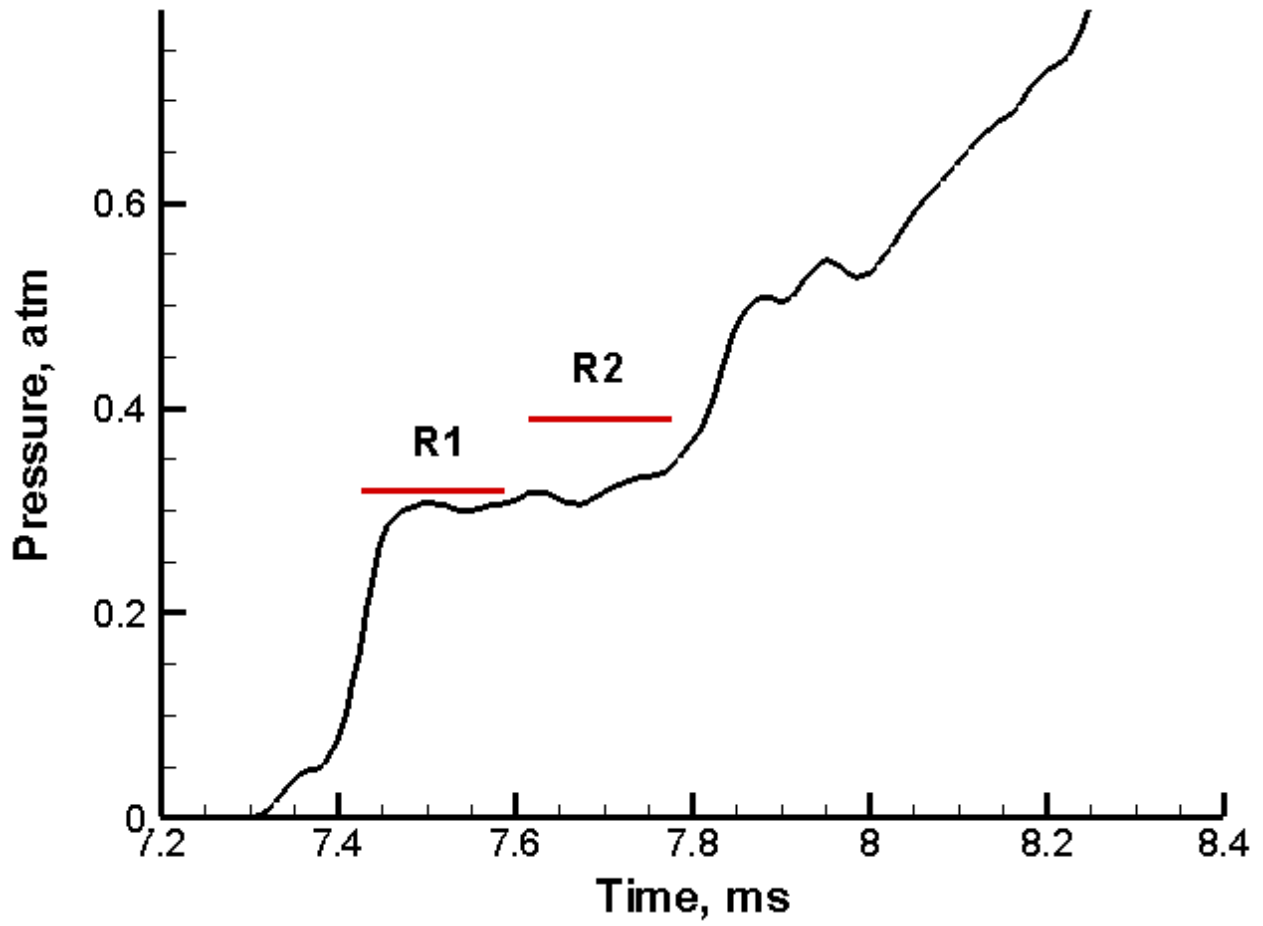


Fig. 2: Time varying pitot pressure during the entire run. Ramp 1 and 2 time durations are shown as red lines.

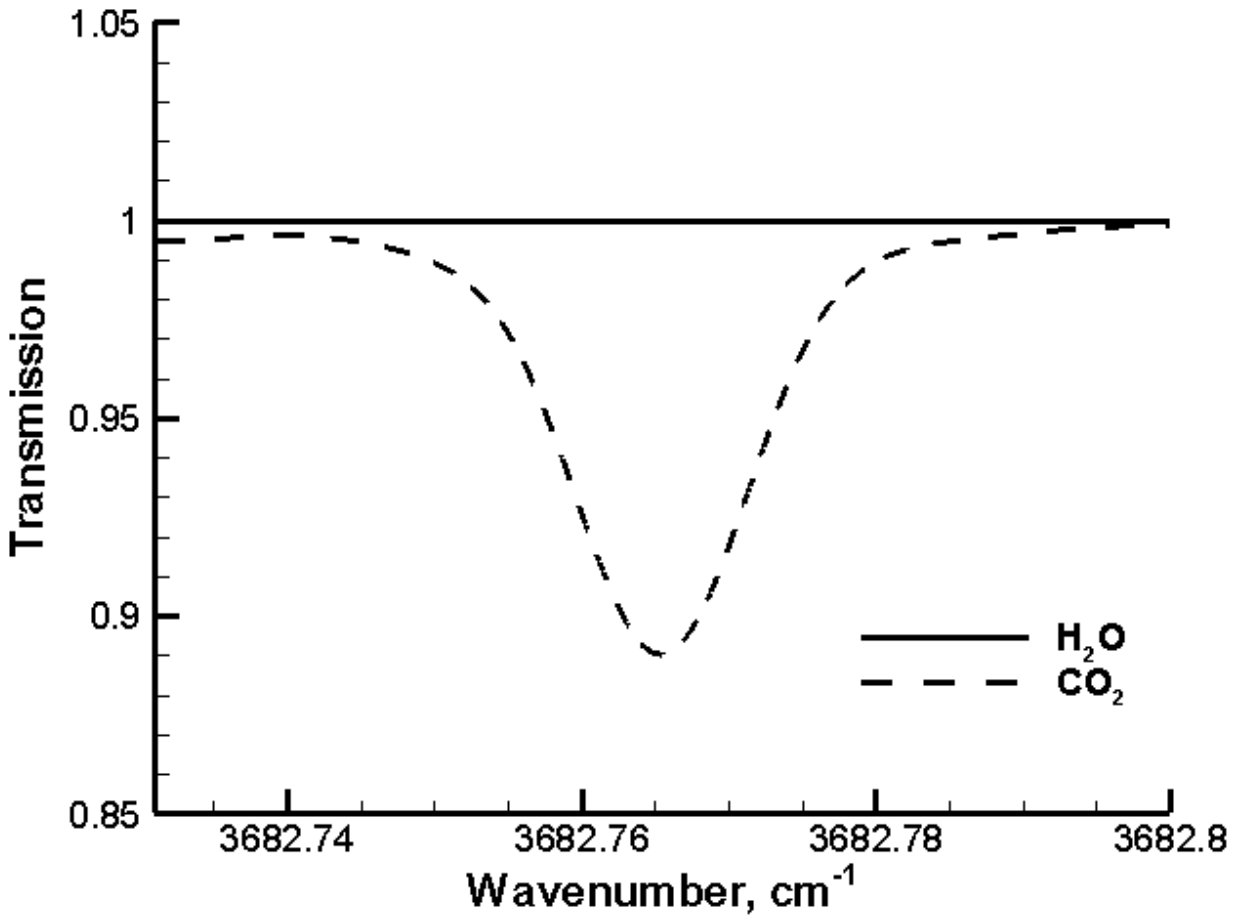


Fig. 3: Transmission plot from simulation of normal run CO₂ levels and nominal laboratory conditions for H₂O experienced during a run.

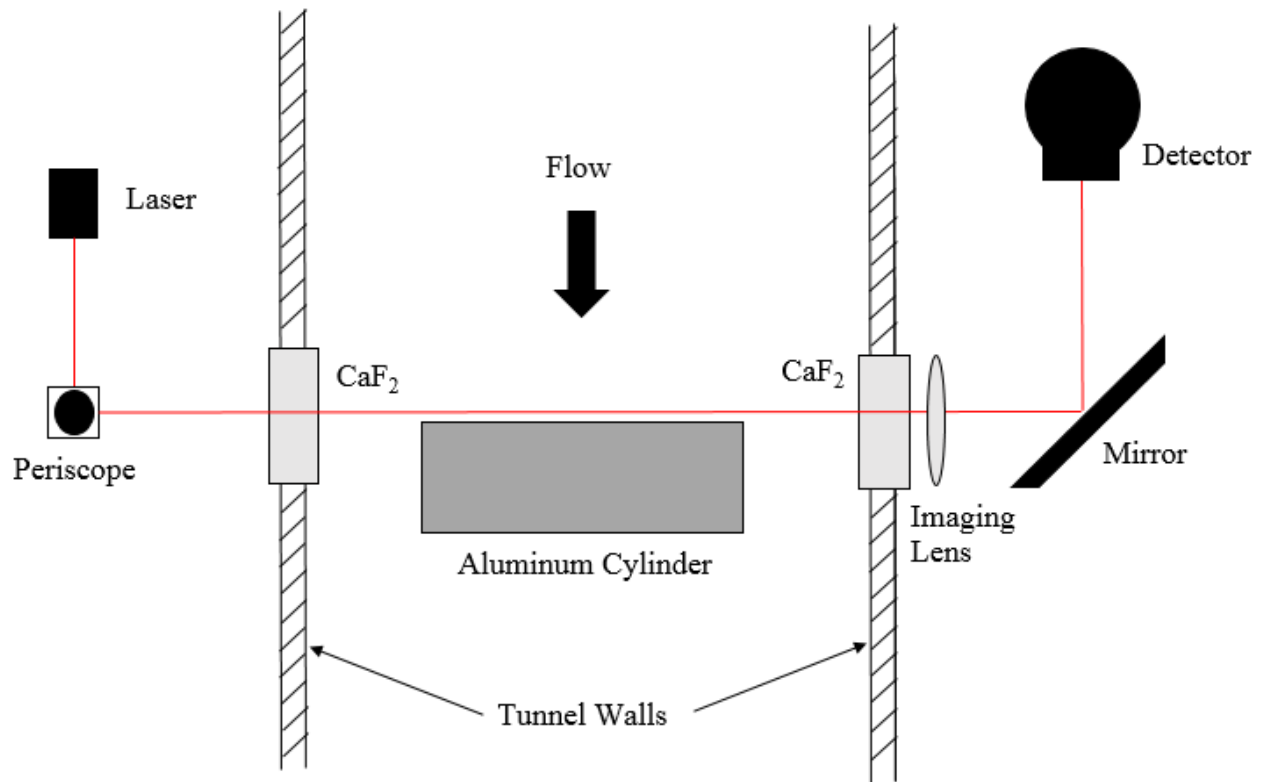


Fig. 4: Top view schematic of experimental optical bench setup.

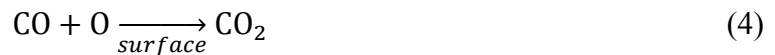
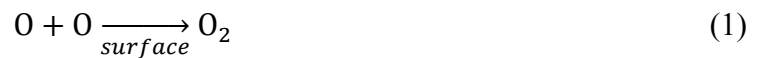
3 Modeling and Data Analysis

3.1 Computational Fluid Dynamics

The Data-Parallel Line Relaxation (DPLR) code, developed by the NASA Ames Research Center, is the tool used for the CFD portion of the analysis of the experiment. DPLR is a multi-block, structured, finite-volume code that solves the reacting Navier-Stokes equations including finite rate chemical and thermal non-equilibrium effects. The code is based on the data-parallel line relaxation method [22] and implements a modified, low-dissipation Steger-Warming flux splitting approach [23] for the convection terms and central differencing for the diffusion terms. Transport properties for the reacting mixtures are modeled in DPLR for high enthalpy flow [24, 25] using the binary collision-integral based mixing rules from Gupta, et al. [26] with a database of relevant collision integral data for high temperature collisions [27, 28]. Diffusion coefficients are modeled using self-consistent effective binary diffusion (SCEBD) [29]. The DPLR code allows an arbitrary set of chemical species and reactions to be used. In this work, a standard eight-species air/carbon dioxide species set (CO_2 , CO , N_2 , O_2 , NO , C , N , O) was employed using the set of reaction rates published by Park, et al [30]. Reverse reactions rates were computed from equilibrium. Finite rate vibrational relaxation is modeled via a simple harmonic oscillator vibrational degree of freedom [31] using the Landau-Teller model [32]. Vibrational energy relaxation rates are computed by default from the semi-empirical expression from Millikan and White [33], but rates from the work of Camac [34] and Park, et al. [30] are substituted for specific collisions where experimental data exists. Vibration-dissociation coupling is currently modeled using the $T - T_v$ approach of Park [35].

The non-catalytic wall boundary condition enforces zero catalytic production for each species, which implies that diffusion flux for each will be zero. The super-catalytic boundary condition sets a mixture composition explicitly at the surface that coincides with the lowest energy composition of the gas without regard for reaction kinetics or reactant availability. The super-catalytic boundary condition enforces a non-physical set of catalytic production rates at the surface, but does provide an upper limit on energy release at the surface and thus a conservative estimate for design of the TPS. The specified reaction efficiency (SRE) model enforces a user-specified efficiency for catalytic reactions based on the fraction of reactant species that reach the surface for which a recombination event occurs. The reaction efficiency (or reactant loss efficiency), γ , may be specified as constant or as a function of temperature resulting from an empirical curve-fit of experimental data. Very recently, a generalized, physics-based finite rate surface chemistry (FRSC) model [36, 37] has been implemented in the DPLR code that allows for an arbitrary number of physical reaction forms such as E-R and L-H recombination events to be specified. The FRSC model requires specification of a large number of physical parameters that must be obtained for each environment and has not yet gained widespread use.

For mixed air/carbon dioxide systems, a number of outcomes affecting the energy balance at the surface are possible, including those listed in Eqs. (1) – (4).



Besides homogeneous atom recombinations, given in Eq. (1) and Eq. (2), heterogeneous recombination producing nitric oxide has been recently suggested as an important surface catalytic mechanism for reacting air [8]. For dominantly carbon dioxide systems, such as would be relevant for Martian entry applications, the competition between Eq. (1) and Eq. (4) for consumption of atomic oxygen results in very different heat flux to the surface [38]. Evidence by Sepka, et al. [39] suggests that Eq. (4) should occur with relatively low efficiency for surfaces at or near room temperature because of the large energy barrier of CO [40]. However, little is known about this mechanism at hypersonic, flight-relevant conditions, and experiments in shock tunnel environments have shown heat flux results that are consistent with highly-efficient CO₂ production at the surface [3, 41]. In this work, the catalytic recombination efficiency parameter is defined in Eq. (5) as the fraction of CO molecules reaching the surface that participate in a recombination to CO₂ via the reaction pathway in Eq. (4). The flux of CO to the surface is obtained via kinetic theory. Each recombination event by Eq. (4) also consumes one oxygen atom, but oxygen atoms are simultaneously consumed by other reaction pathways (e.g. Eq. (1) and Eq. (3)). Molar consumption of CO and molar production of CO₂, however, are clearly linked in a 1:1 ratio by Eq. (4). The recombination efficiency parameter is defined in Eq. (5) as the negative of the CO molar production rate over the CO impingement flux. Its value ranges from zero to unity.

$$\gamma_{cat} = \frac{-\dot{w}_{CO}}{\Gamma_{CO}} = \frac{-\dot{w}_4}{\Gamma_{CO}} \quad (5)$$

This surface catalysis model is not limited by the assumption of particular site balance reaction models, such as the L-H or E-R models. However, the drawback is that the value of the recombination efficiency parameter has an unknown dependency on factors such as temperature, densities, and surface conditions.

Because the test gas is a mixture of air and carbon dioxide that will be dissociated in the shock layer, several catalytic outcomes are possible for the near surface region. Downstream of the bow shock in the stagnation region, the calculation of the equilibrium state of the gas is $T_{eq} = 4425 K$, $P_{eq} = 30.3 kPa$, $Y_{N_2,eq} = 0.493$, $Y_{O_2,eq} = 0.006$, $Y_{NO,eq} = 0.020$, $Y_{N,eq} = 0.005$, $Y_{O,eq} = 0.261$, $Y_{CO_2,eq} = 0.001$, and $Y_{CO,eq} = 0.214$. Although some boundary layer recombination will certainly occur, the gas approaching the surface will be largely composed of carbon monoxide, atomic oxygen, and molecular nitrogen at these conditions.

Although this experiment does not identify a specific physical mechanism through which a surface reaction occurs, it does provide, to the author's best knowledge, the first direct measurement of the effectiveness of the major reaction pathway described by Eq. (4) at a flight relevant freestream velocity. The consumption of atomic oxygen cannot be directly analyzed using the measured data in this case, but the reactant loss efficiency of carbon monoxide can be directly fit from the measured data using the techniques outlined here. This effort, therefore, represents a major advancement over the current non-physical observations made from high enthalpy facilities by interpreting indirect measurements such as heat flux, surface temperature, or recession rates that are non-linear functions of multiple simultaneous processes that cannot be easily decoupled.

3.2 Line-by-Line Model

The theory behind absorption spectroscopy is based on the Beer-Lambert law, which governs the absorption of monochromatic radiation through weakly absorbing homogeneous medium.

$$\frac{I}{I_0} = \exp(-k_\nu L) \quad (6)$$

The spectral absorption coefficient is defined as,

$$k_\nu = S_i(T)PX\varphi_\nu \quad (7)$$

Reference linestrength data at 296 K was obtained from the HITRAN 2008 database [42].

Linestrengths were scaled to other temperatures with the following relation,

$$S_i(T) = S_i(T_o) \frac{Q(T_o)}{Q(T)} \left(\frac{T_o}{T}\right) \exp\left[-\frac{hcE''}{k} \left(\frac{1}{T} - \frac{1}{T_o}\right)\right] \left[1 - \exp\left(\frac{-hc\nu}{kT}\right)\right] \left[1 - \exp\left(\frac{-hc\nu}{kT_o}\right)\right]^{-1} \quad (8)$$

A third order polynomial is used to fit the partition function from the given data in the HITRAN database. The lineshape, φ_ν , is a function of multiple types of broadening mechanisms, some more important than others. The two dominating mechanisms in this study are Doppler broadening and collisional broadening, with typical full-width at half-maximum (FWHM) values of approximately 0.012 cm^{-1} and 0.046 cm^{-1} , respectively. Doppler broadening is caused by the random thermal motion of the absorbing molecules and follows a Maxwellian velocity distribution, resulting in a Gaussian lineshape.

$$\varphi_D(\nu) = \frac{2}{\Delta\nu_D} \left(\frac{\ln(2)}{\pi}\right)^{1/2} \exp\left[-4\ln(2) \left(\frac{\nu-\nu_o}{\Delta\nu_D}\right)^2\right] \quad (9)$$

The Doppler FWHM is given below, where the final expression is simplified from the intermediate expression to work in wavenumber units.

$$\Delta\nu_D = \nu_o \left[\frac{8kT\ln(2)}{mc^2}\right]^{1/2} = 7.1623 \times 10^{-7} \left[\nu_o \left(\frac{T}{M}\right)^{1/2}\right] \quad (10)$$

Collisional broadening occurs when molecules collide with each other and is modeled using the Lorentzian function. It is assumed that the collisions are binary and that the collision duration is negligible compared to the time between collisions, and is given by,

$$\varphi_C(\nu) = \frac{1}{\pi} \frac{\frac{\Delta\nu_C}{2}}{(\nu - \nu_o)^2 + \left(\frac{\Delta\nu_C}{2}\right)^2} \quad (11)$$

The collisional FWHM is given by the expression,

$$\Delta\nu_C = 2P \left(\frac{T_o}{T}\right)^n [X\delta_{self} + (1 - X)\delta_{air}] \quad (12)$$

The self-broadening half-width and air-broadening half-width are obtained from the HITRAN database. Doppler broadening is dominant at lower pressure, while at higher pressures, collisional broadening is dominant. The Doppler and collisional FWHM values are comparable, and a Voigt profile is needed that describes the convolution of the two lineshapes. An approximate model of the full frequency-space convolution is used in this study [43].

3.3 Raw Data Analysis

The raw data obtained from the data acquisition system is processed to obtain a plot of transmission versus wavenumber for comparison to simulations. The raw data is measured in volts on the y-axis and time on the x-axis. The voltage is arbitrary and depends on the setup parameters for the laser and detector. The raw data between 5 and 9 *ms* from the run can be seen in Fig. 5. Two of the sawtooth ramps (1 and 2) are investigated further in this paper. Ramp 1 occurs between 7.426 and 7.588 *ms*, and ramp 2 occurs between 7.616 and 7.777 *ms*.

The process used to reduce the raw data to transmission data is shown graphically in Fig. 6. The raw data is first trimmed down to a single ramp (black data). Data just before and after the ramp when the laser is below threshold is included in order to subtract out the background. The entire data set is shifted so that all voltages are positive (red data). A linear fit between the pre- and post-ramp data is used to subtract out the background (dashed red line). The resulting data (blue data) is used to obtain the transmission plot. The background and baseline portions of the

data set can be seen in Fig. 7. The baseline is the portion of the data when the laser is above threshold, but the gas is not absorbing. A least squares fit for a third order polynomial is used to initially fit the baseline. A non-linear Chi-squared minimization is then performed to fit a combination of the baseline and absorption feature. The fitting process is iterated using varying baseline bounds until a minimum Chi-squared is converged upon. The polynomial, Lorentz, and Gaussian functions can be seen in Eqs. (13-15) below, where the values of the coefficients a_n are varied until the best fit is obtained using the method described above.

$$f_{polynomial}(a_1, a_2, a_3) = a_1 + a_2x + a_3x^2 + a_4x^3 \quad (13)$$

$$f_{Lorentzian}(a_4, a_5, a_6) = \frac{\left(\frac{a_4 a_5}{2\pi}\right)}{(x_i - a_6)^2 + \left(\frac{a_5}{2}\right)^2} \quad (14)$$

$$f_{Gaussian}(a_7, a_8, a_9) = \sqrt{\frac{4 \ln 2}{\pi}} \left(\frac{a_7}{a_8}\right) \exp \left[-4 \ln 2 \left(\frac{x_i - a_9}{a_8}\right)^2 \right] \quad (15)$$

The baseline is then divided out and the transmission spectrum is obtained. The y-axis values are the unitless transmission, while the x-axis values are still in an arbitrary index. A wavenumber calibration is needed to transform the x-axis index to wavenumber units.

The wavenumber calibration is obtained using a test cell of known temperature, pressure, path length, and concentration. The test cell used is the actual expansion tube where the main tests are taking place. The section is first pumped down to approximately 25 *mTorr*. At this level of vacuum, there is still some H₂O in the test section. Pure CO₂ is then squirted into the test section until the pressure rises to approximately 55 *mTorr*, at which point the test cell measurements are taken. A simulation using the test cell parameters is generated, and the slope of the wavenumber calibration ($cm^{-1}/index$) is adjusted until the raw data matches the simulation data. The only unknown in the process is the calibration slope itself. An example of the calibration fit can be seen in Fig. 8. The slope of the wavenumber calibration used in the following data analysis is -8.479 x

$10^{-5} \text{ cm}^{-1}/\text{index}$. The negative sign is needed because as the laser current is increased, the wavelength increases, which corresponds to a decrease in wavenumber. Pre-test data was taken over a range of 35 *ms* to measure the stability of the laser and its wavenumber calibration. A plot of the full-width half-maximum for an arbitrary 15 *ms* in the pre-test data can be seen in Fig. 9.

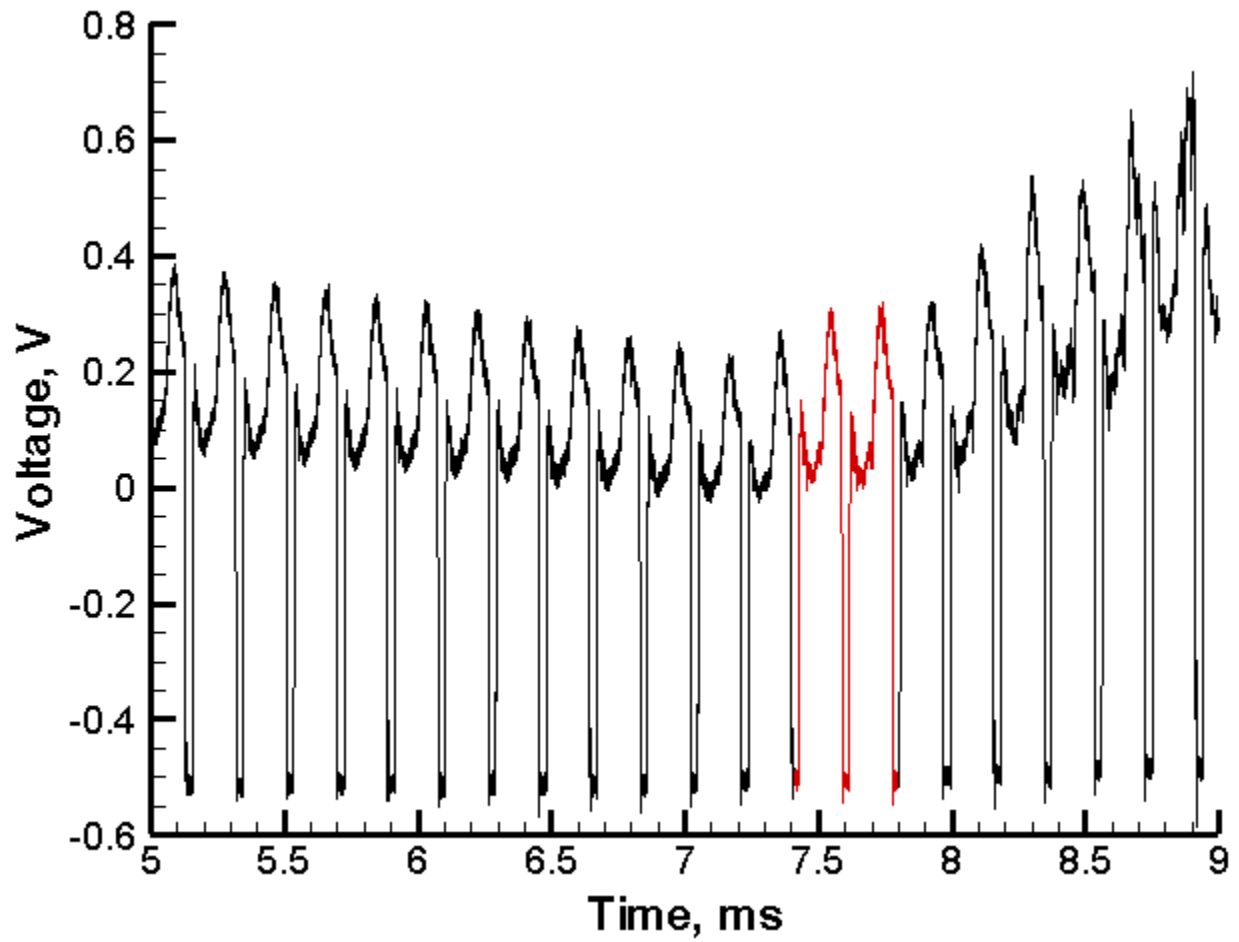


Fig. 5: Portion of raw data from run, with ramps 1 and 2 highlighted in red.

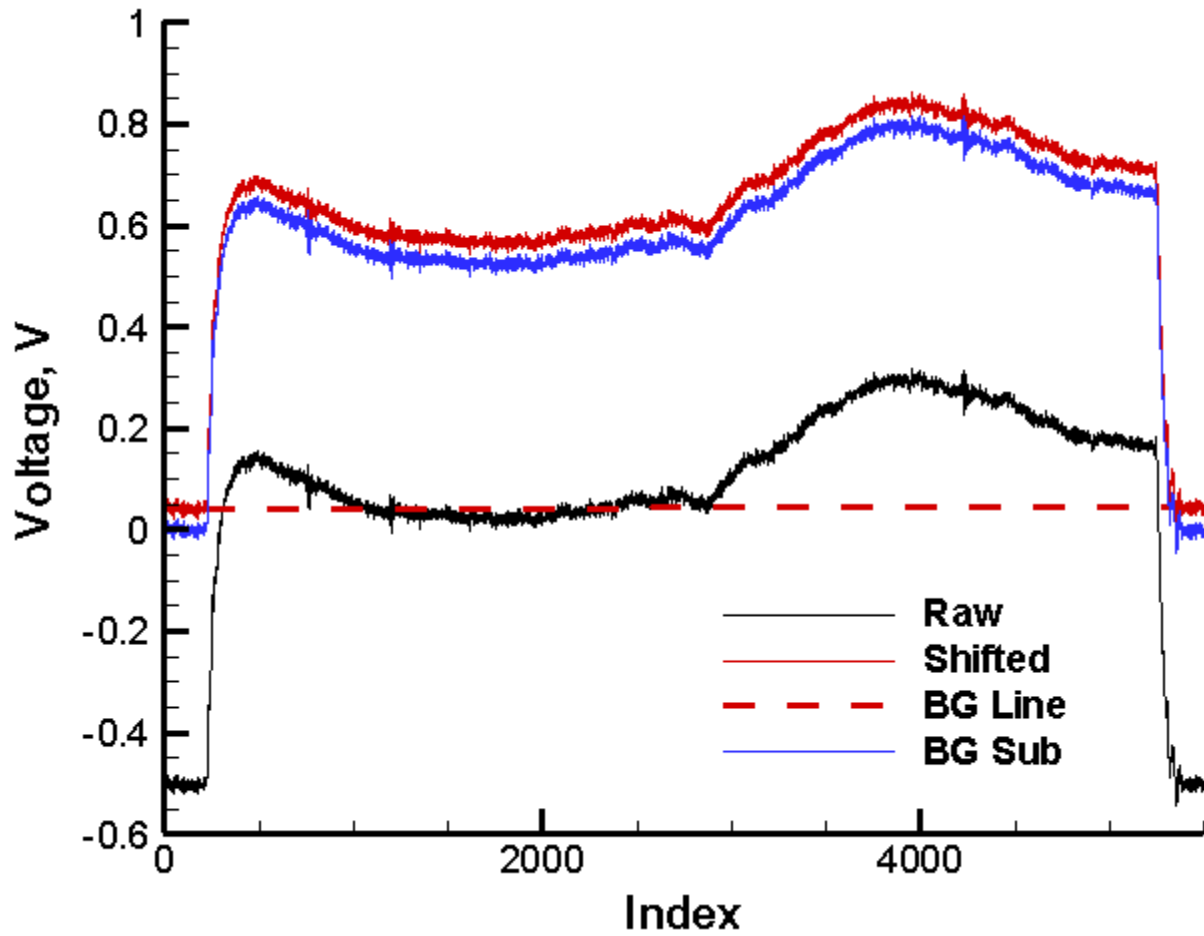


Fig. 6: Transformation of single raw data ramp to transmission data.

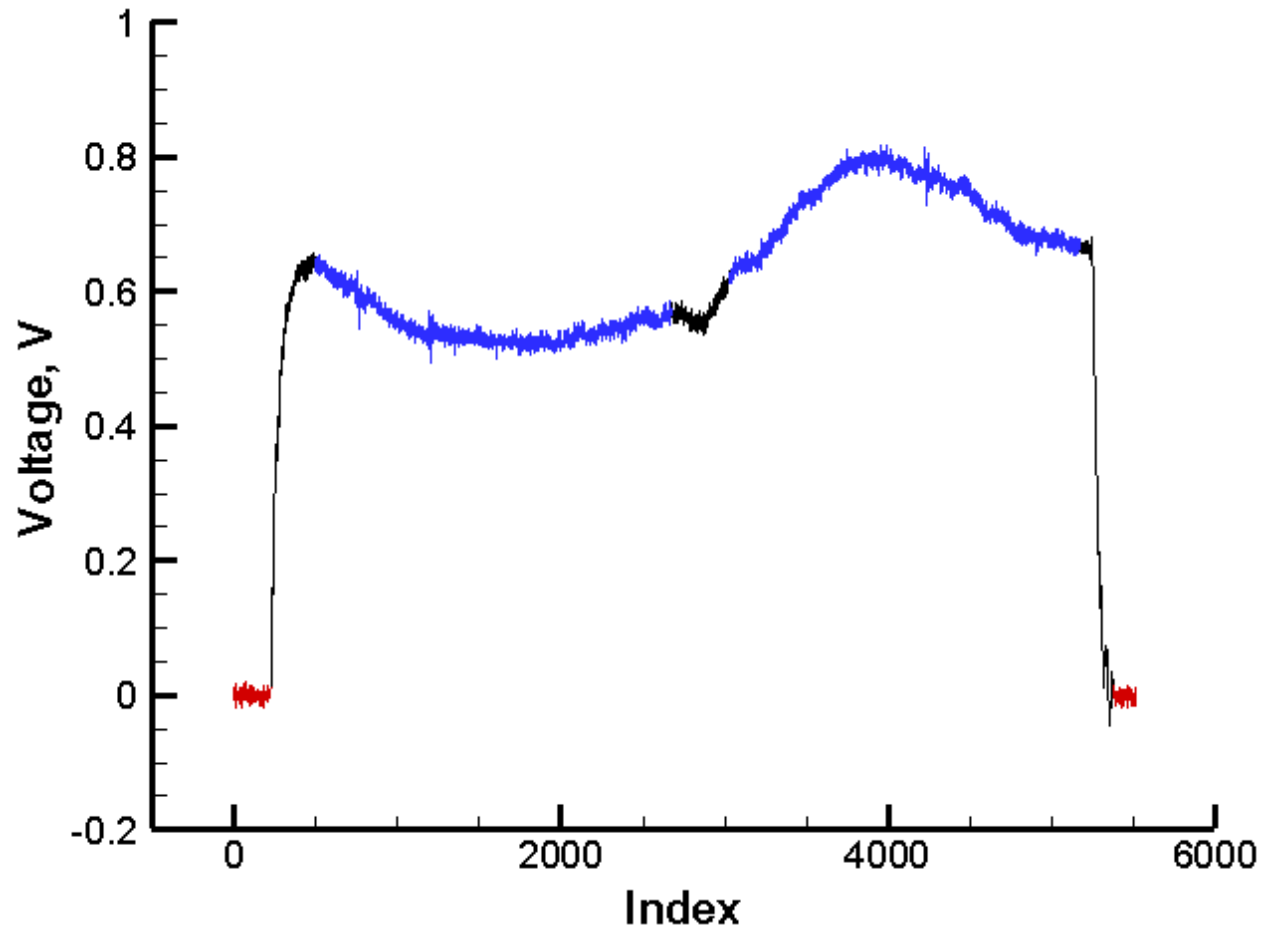


Fig. 7: Background (red) and baseline (blue) used to transform raw data to transmission data.

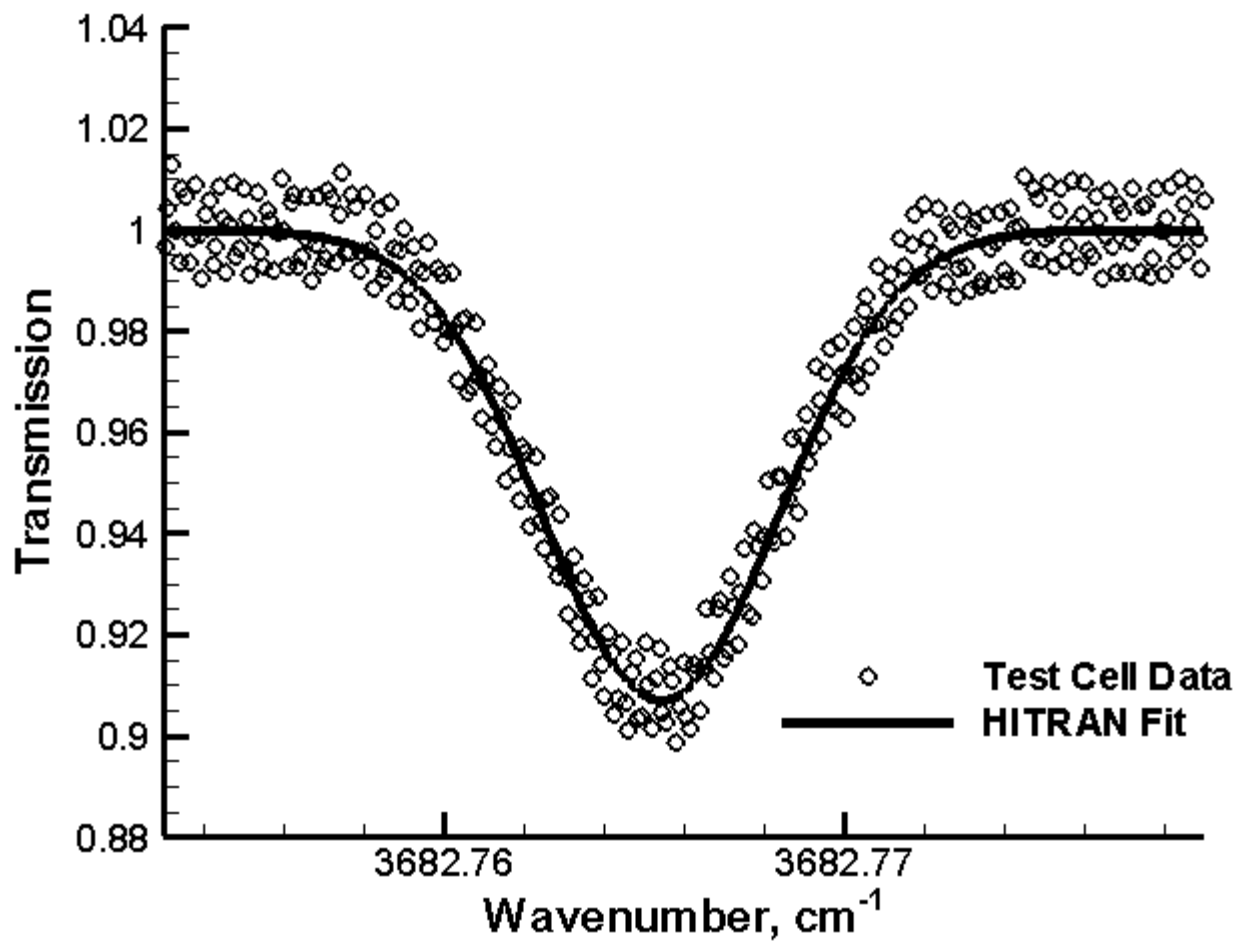


Fig. 8: Example wavenumber calibration showing raw data along with HITRAN simulation fit.

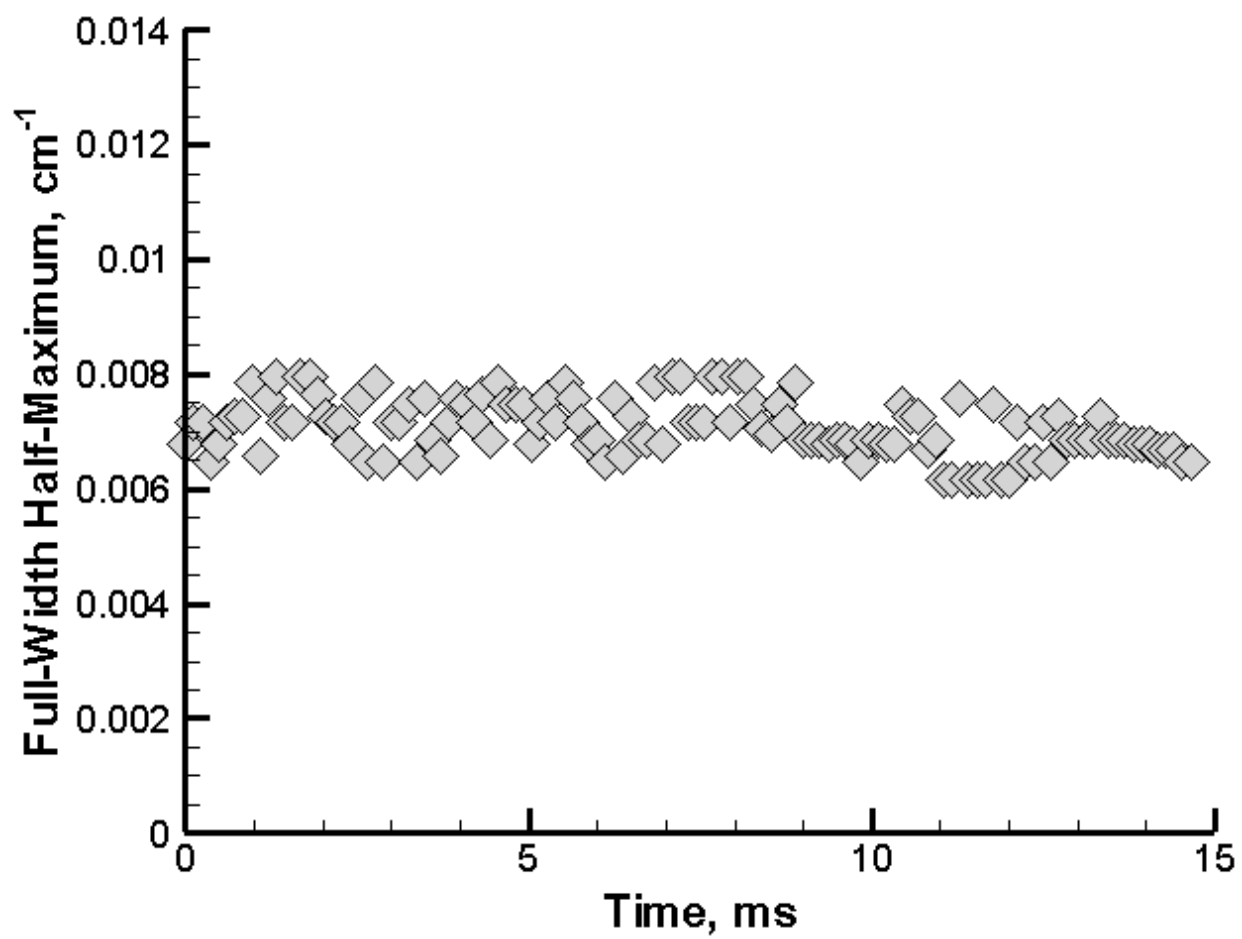


Fig. 9: Pre-run full-width half-maximums of wavenumber calibration.

4 Results and Discussion

4.1 CFD and LBL Modeling

An idealized, unsteady, axisymmetric CFD simulation of the entire expansion tunnel is used to obtain the freestream mole fraction, normalized temperature, and normalized pressure profiles across the tunnel radius. Centerline values are predicted for the test time using the CUBRC High Enthalpy Expansion Tunnel Analysis (CHEETAh) code [19]. The normalized profiles are then re-dimensionalized using the centerline values so that non-ideal effects such as diaphragm breaking are accounted for. This simulation accurately captures the boundary layer along the expansion tunnel wall, which has an impact on the overall simulation absorption profile. A plot of these profiles can be seen in Fig. 10. The temperature and pressure profiles used in the simulations are found by multiplying the normalized profiles by the freestream values given in Section 2.1.

Property data for the LBL method is extracted from the CFD solutions. The extraction procedure interpolates between cells because the curvilinear cells are not necessarily aligned with the straight laser beam path. For each line-of-sight, the extracted data points include two freestream sections, two expanding flow sections, and the cylinder surface section, as seen in Fig. 11. The locations of the line-of-sight extraction points depend on the size of the detector element, the distance the element is off the cylinder surface, and the angle of the element above the stagnation line. The plots in Fig. 12 show the shock layer solutions of temperature, pressure, and mole fraction for both the non-catalytic and super-catalytic cases along the stagnation line. The most notable change between the two solutions is the mole fraction of CO_2 . For the super-catalytic

case, the mole fraction at the surface returns to the freestream value. The mole fraction for the non-catalytic case is significantly lower. The pressure is relatively constant throughout the entire shock layer, as is the temperature until it drops down to the aluminum cylinder cold-wall temperature of 300 K; the test times in an expansion tunnel are so short that the material does not have enough time to accommodate to the temperature of the gas behind the shock. The absorption line that is investigated is a low temperature line; as temperature increases, the absorption decreases. The selected transition ensures that detection of CO₂ is more probable near the cylinder surface due to its sensitivity to low temperatures.

The LBL code uses the methodology in Section 3.2 to simulate each line-of-sight. The properties of the gas change throughout the line-of-sight, and it must therefore be split into homogeneous zones in order for the Beer-Lambert law to hold. This leads to a discretized form of Eq. (6) in which the transmitted intensity from one homogeneous zone is used as the incident intensity for the next homogeneous zone. The individual lines-of-sight are finally averaged together to simulate the entire detector element. A flowchart of the solution procedure can be seen in Fig. 13.

4.2 Sensitivity Studies

The experimental setup is constructed and documented as well as possible, but there is always a chance that some parameter varies slightly between the setup and the run. This section investigates the effects of slight perturbations from nominal conditions and their impact on the overall absorption spectrum. The base conditions used for each sensitivity study are a detector element width of 80 μm located at five degrees above the stagnation line and 40 μm off the cylinder surface. Twenty polyline points normal to the cylinder surface are used for simulation in each case, except for the polyline point sensitivity case. The sensitivity studies investigate the

following: detector element point independence, element size, element distance off the surface, element angle above the stagnation line, simulated element size, and expanding flow around the cylinder edge. A schematic illustrating these cases can be seen in Fig. 14.

The number of data points extracted from the CFD solution for use in the LBL simulation can range anywhere from a single point to hundreds of points. Plots of the transmission versus wavenumber are used to determine the minimum number of lines-of-sight that can be used in a simulation to obtain an accurate result. Lower numbers of points reduce computational time, but accuracy of the solution suffers. A plot of the spectra generated from the LBL code for varying numbers of lines-of-sight can be seen in Fig. 15. There is less than 0.5% difference between using 20 points and 25 points, so 20 lines-of-sight are used for simulations for the remainder of the study.

The size of the detector element is determined before the run. With knowledge of the magnification of the optical system, the imaged size of each detector element is determined from the actual element dimension. A screw with known thread pitch is placed along the surface of the cylinder in the laser beam path and imaged onto an IR camera. A hollow tube is also placed in the flow adjacent to the surface. Both the screw and tube can be seen adjacent to the cylinder in the image in Fig. 16. The hollow tube has an outer diameter of 1.4732 millimeters and inner diameter of 1.1684 millimeters. The wall thickness in the image is nearly uniform indicating good alignment along the entire cylinder surface. Using information from both the hollow tube and the screw, a calibration of the IR camera pixel element to physical distance is made. The magnification is then determined, and applied to the pixel element of the 32-element IR detector. The detector element width is $250 \mu\text{m}$. Accounting for 3.125x magnification, the apparent size of the element in the flow is $80 \mu\text{m}$. Pixel sizes of 70, 80, 83, and $90 \mu\text{m}$ are compared to investigate the effects

on the total transmission, which can be seen in Fig. 17. The maximum percent difference between the spectra for the non-catalytic case is 0.15%, and for the super-catalytic is 1.47%.

When using a multi-element (linear array) detector, the detector elements extend out from the cylinder surface into the flow. It is possible that the near-surface element is displaced from the surface of the cylinder out into the shock layer some distance, on the order of tens of microns. The transmission plots for both non-catalytic and super-catalytic simulations can be seen in Fig. 18. The high temperature P48f transition can be seen at approximately 3682.73 cm^{-1} in these simulations, but is lost in the noise of the raw data due to its low absorption. The measurement is sensitive to distances off the cylinder surface, more so for the super-catalytic case because the gradient of CO₂ mole fraction is large compared to the non-catalytic case. The maximum percent difference between the transmission plots for the non-catalytic and super-catalytic cases is 5.2% and 36.7%, respectively. The percent difference for $\gamma = 0.00025$ and $\gamma = 0.0005$ is 6.39% and 7.62%, respectively. These two cases are the best fit catalytic efficiencies for ramp 1 and 2 described in Section 4.3. It is therefore imperative to accurately measure the distance of the detector element off the surface of the cylinder.

The effect of angular location above the stagnation line on the transmission spectrum is evaluated for angles of 0, 5, 10, 15, and 20 degrees. An angle of 0 degrees indicates an element on the stagnation line. As the angle increases, the transmission decreases (as more light is absorbed), though not significantly. The transmission plots for the various angles can be seen in Fig. 19. The maximum percent difference between the spectra for the non-catalytic and super-catalytic cases is 0.15% and 1.58%, respectively.

When extracting data from the CFD simulations, the height of the detector element has up until now been neglected because the property gradients are small along the vertical direction (radially

around the cylinder). It was shown that 20 lines-of-sight along the horizontal direction of the detector element (perpendicular out from the cylinder surface) is sufficient to accurately simulate the flow. The first case is the 20x1 element simulation, in which 20 points are taken along the horizontal pixel direction (along the width). The second case is the 20x5 simulation, in which 20 points are taken along the horizontal direction at five vertical locations (along the height). The transmission plots for both cases can be seen in Fig. 20. The maximum percent difference between the transmission curves for non-catalytic and super-catalytic cases is 0.02% and 0.03%, respectively. The small differences indicate that the 20x1 method is sufficiently accurate for all simulations.

In 3D flow around a cylinder, effects that are not seen in a simple 2D simulation are introduced. One of these effects that has the potential to be important is the expanding flow around the edges of the cylinder. As the flow moves around the edges, the concentration changes along with pressure and temperature. The expansion section decreases the amount of freestream the laser travels through. However, it now needs to travel through this expansion region on both sides of the cylinder. Depending on the physical and chemical makeup of the gas, this region might increase the absorption through the path length. The path length the laser travels through the expanding flow on one side of the cylinder is 0.41 *cm* for the non-catalytic case and 0.49 *cm* for the super-catalytic case. Therefore, the total path length lost by the freestream to the expanding flow is 0.82 *cm* and 0.98 *cm* for the non-catalytic and super-catalytic cases, respectively. The effect of including the expanding flow in the simulations on the transmission spectra is less than 0.1%, and can be ignored.

4.3 Data and Simulation Comparison Results

With temperature and pressure profiles that are nearly the same in the shock layer for any recombination efficiency, the main sensitivity between absorption simulations is the concentration of CO₂. A plot of the stagnation line profiles of the mole fraction of CO₂ in the shock layer for different reaction efficiencies can be seen in Fig. 21. There is a unique mole fraction profile for each reaction efficiency. Because of the particular absorption line selected, the maximum absorption sensitivity occurs immediately adjacent to the surface where the gas temperature is closest to the surface temperature of 300 K. The temperature sensitivity of the absorption line for arbitrary conditions can be seen in Fig. 22. If the exact size and position of the detector element in the flow-field is known, the simulations are able to determine which reaction efficiency produces CFD results that match the experimental data.

The LBL model simulates the cylinder region with a freestream region on each side of the cylinder. To compare the fit of the simulated results to the experimental data, the root mean square (RMS) of the residual between the calculation and the measured data points is computed. A plot of these values for each of the reaction efficiencies (0 (NC), 0.00005, 0.000075, 0.0001, 0.000175, 0.00025, 0.00035, 0.0004, 0.0005, 0.0006, 0.0007, 0.00075, 0.001, 0.00125, and 0.0015) is shown in Fig. 23. The minimum RMS gives the best fit of simulation to raw data. The consistency in the raw data from ramp 1 to ramp 2 indicates a steady measurement during the test time. Specified reaction efficiencies of 0.00025 and 0.0005 for ramp 1 and ramp 2, respectively, provide the best fit to the experimental data.

The plot in Fig. 24 shows the results for the non-catalytic, super-catalytic, and the best fit reaction efficiency of 0.00025 for ramp 1, the first ramp after the arrival of the test gas. The plot in Fig. 25 shows the results for the non-catalytic, super-catalytic, and the best fit reaction efficiency

of 0.0005 for ramp 2, which was measured 250 microseconds later. These best fit results agree with heat transfer distribution data observed indirectly in other experiments in LENS-XX, which has showed a low efficiency of surface catalysis in general and specifically for the CO + O mechanism [2, 44]. This finding and others indicate that the design of TPS based on a super-catalytic boundary condition consistent with measurements made in previous ground test studies may have resulted in an overly conservative heat shield design. The experimental methods used in this study can be applied to different atmospheric compositions and different model materials. This flexibility for the measurements can prove useful for future catalytic measurements.

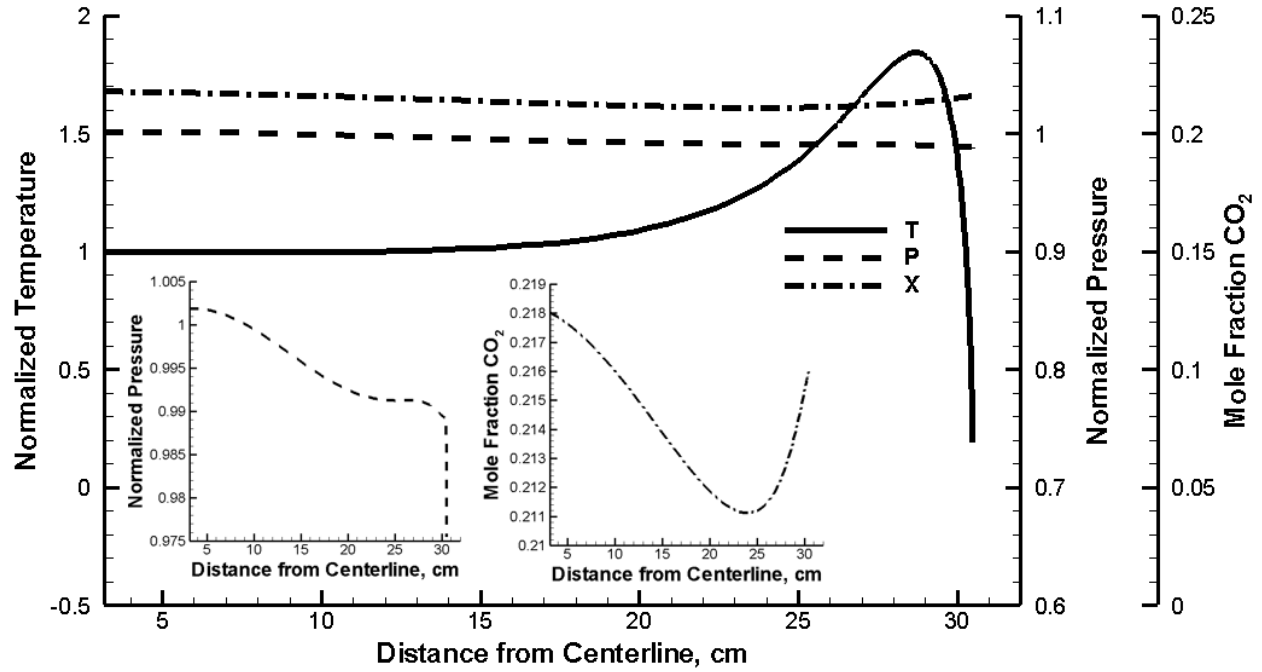


Fig. 10: Normalized temperature, normalized pressure, and mole fraction freestream profiles for half the width of the expansion tube. The two insets show detail of the contour shape for both normalized pressure and mole fraction of CO₂.

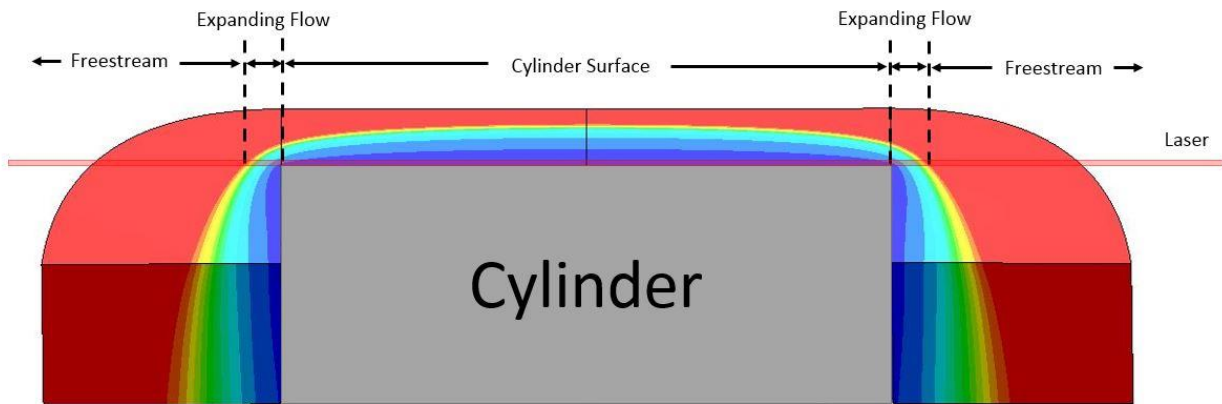
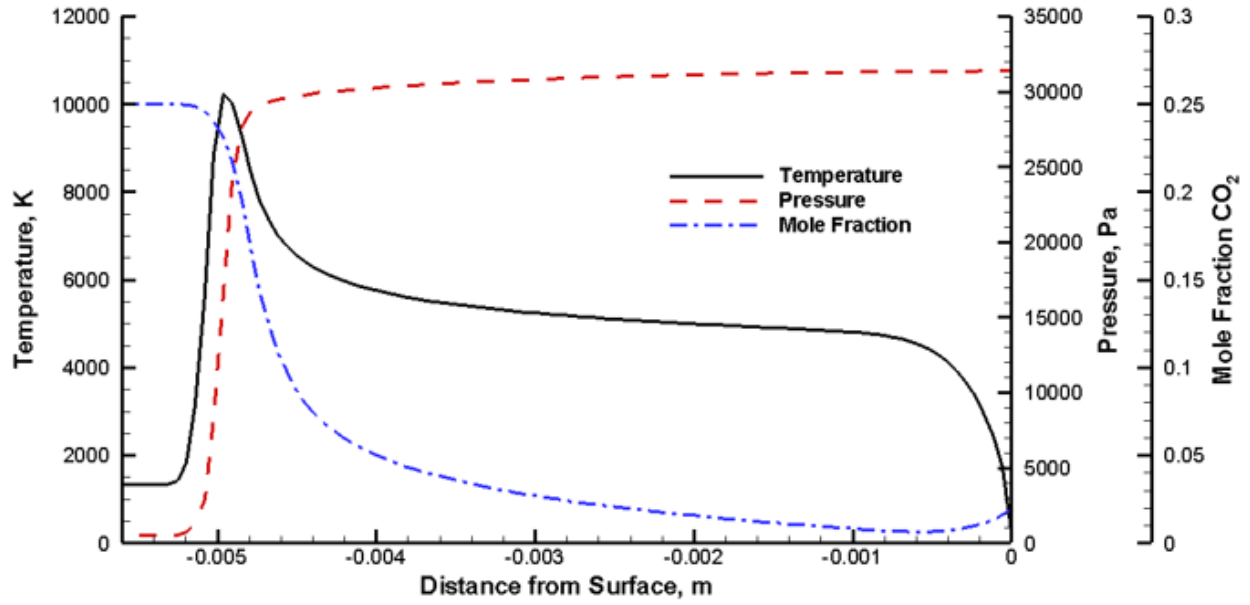
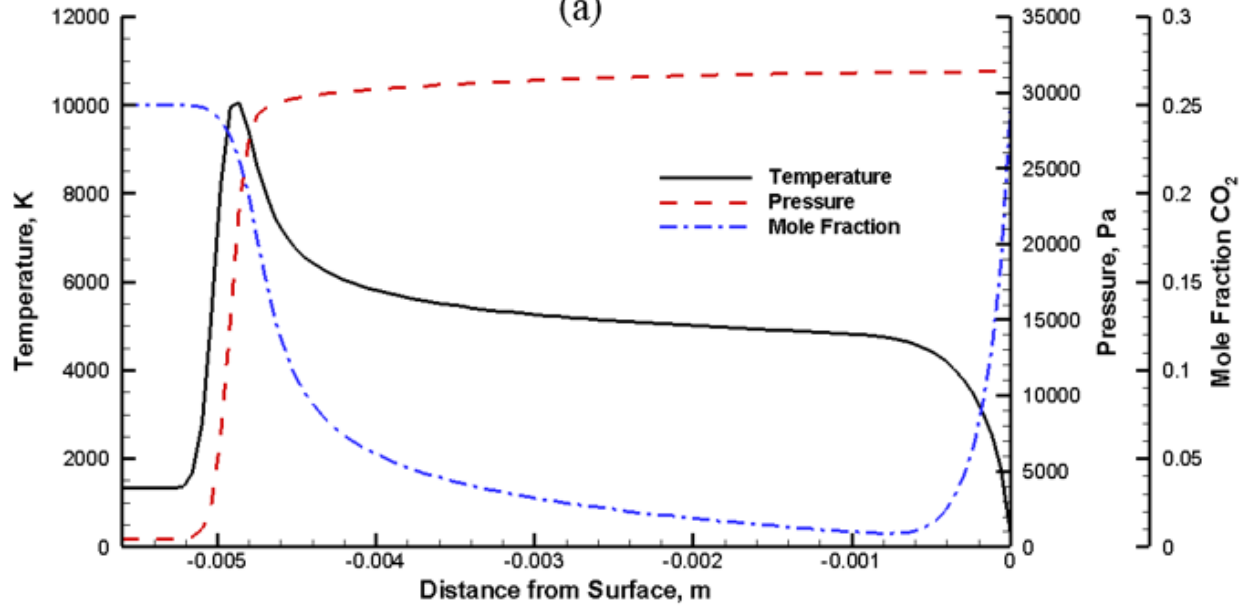


Fig. 11: Schematic of top view of cylinder flow cut along stagnation line with appropriate regions labeled, including freestream, expanding flow, and surface flows.



(a)



(b)

Fig. 12: Shock layer profiles for temperature, pressure, and mole fraction for both the (a) non-catalytic and (b) super-catalytic cases.

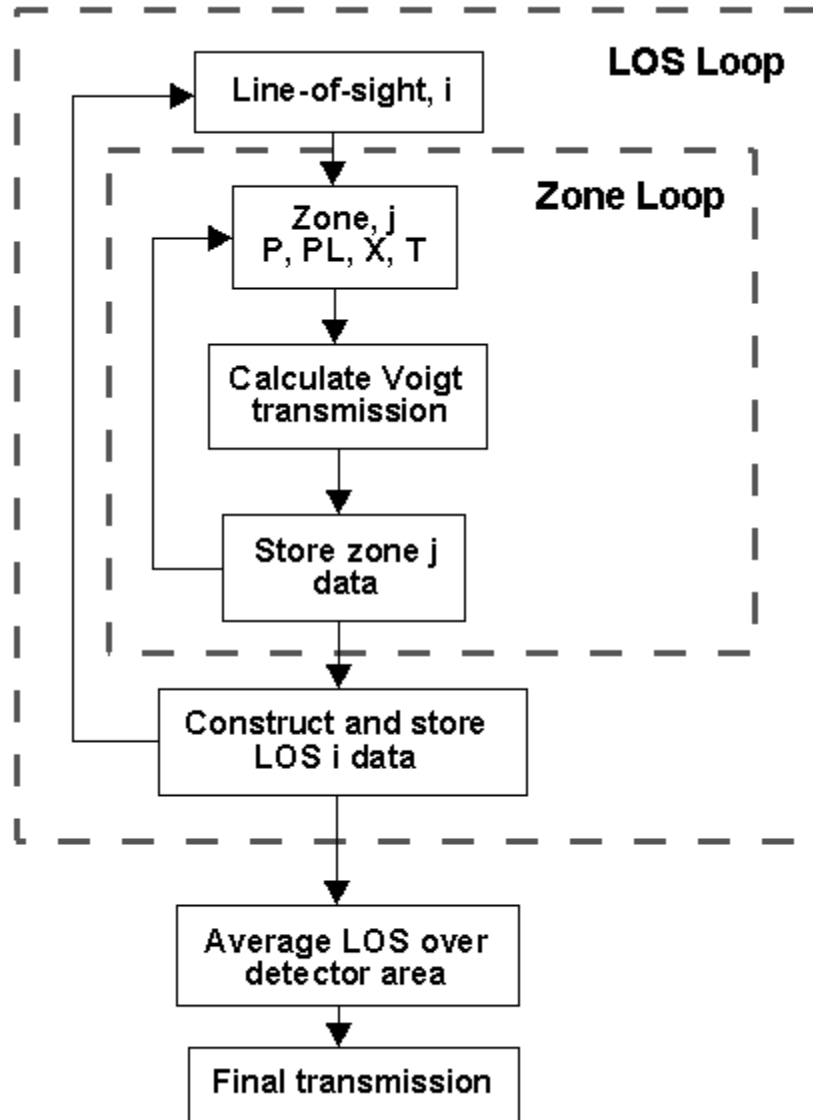


Fig. 13: Flowchart for the line-by-line transmission spectrum simulation code.

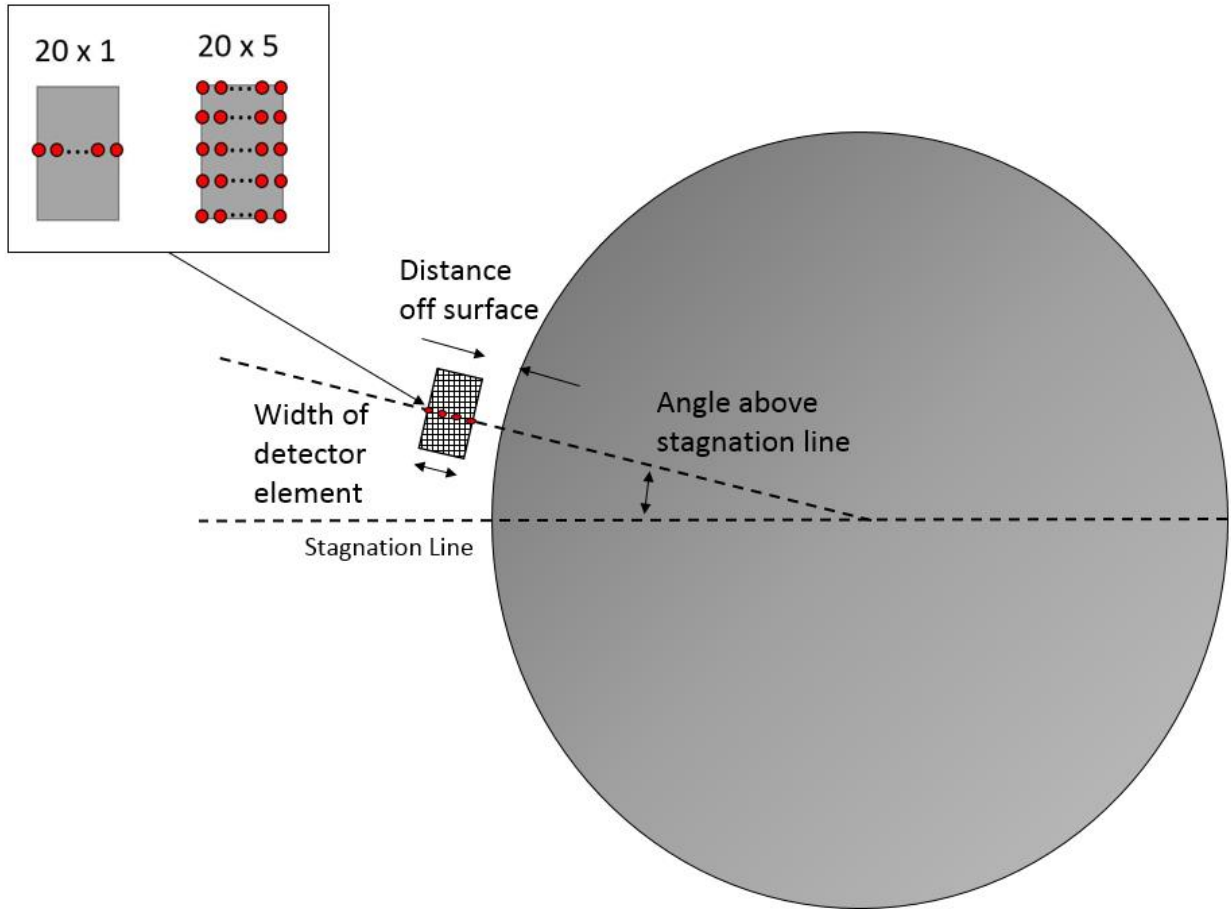


Fig. 14: Schematic for sensitivity studies showing stagnation line angle, element width, and element distance off the surface of the cylinder. The inset shows a schematic for the number of simulated points on the detector element.

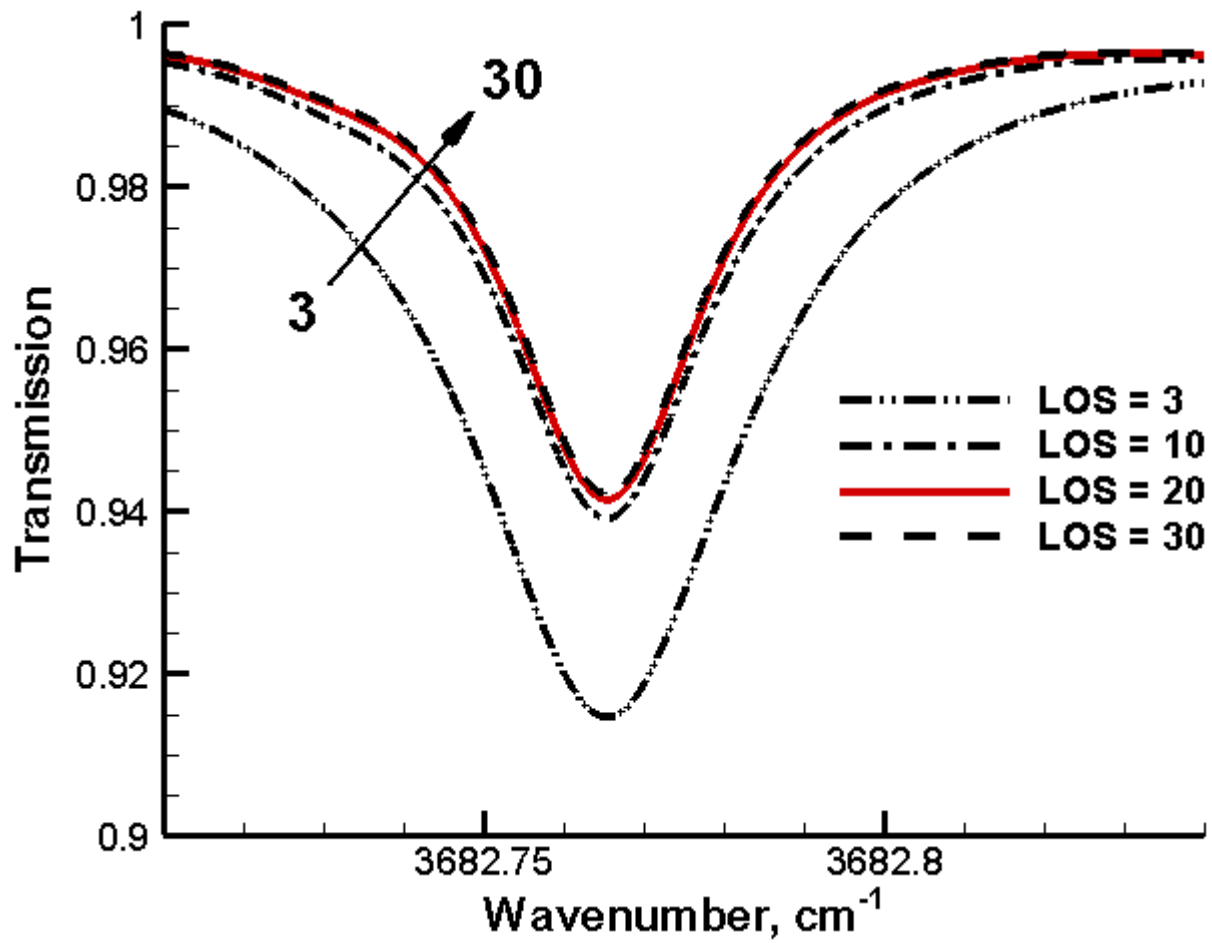
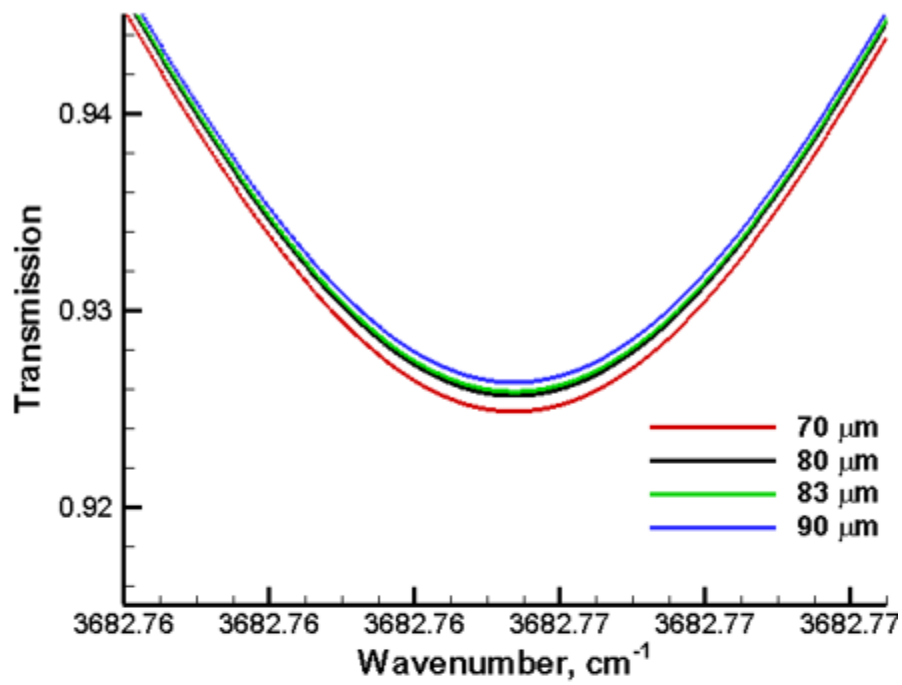


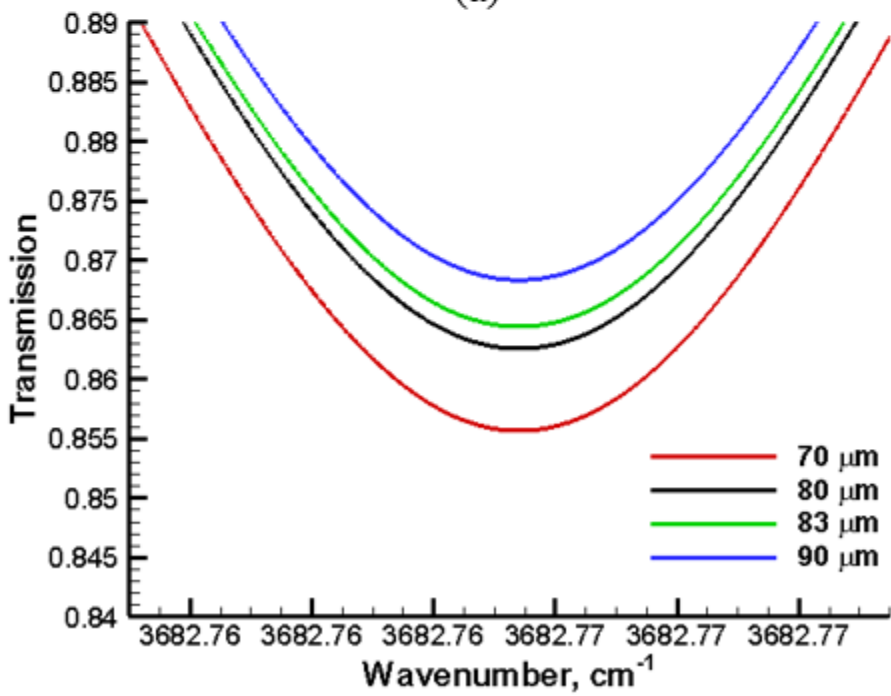
Fig. 15: Transmission plots for various number of polyline points extracted from the CFD results.



Fig. 16: Screw and hollow tube placed adjacent to cylinder for magnification measurement.



(a)



(b)

Fig. 17: Pixel size transmission comparisons for (a) non-catalytic cases and (b) super-catalytic cases.

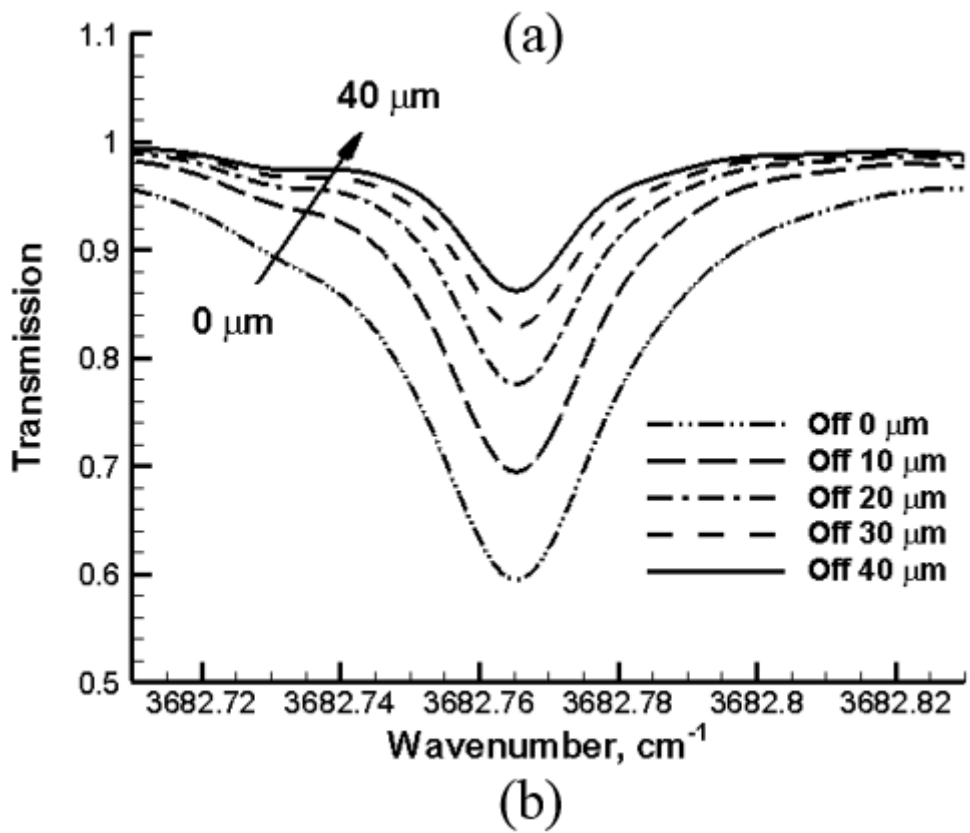
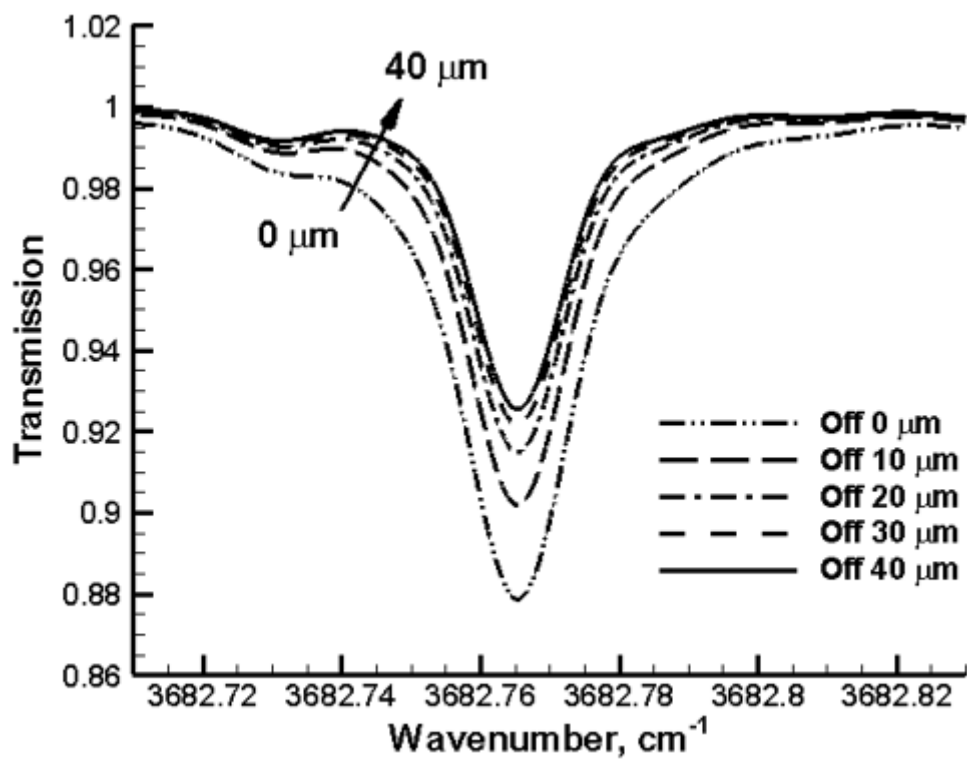
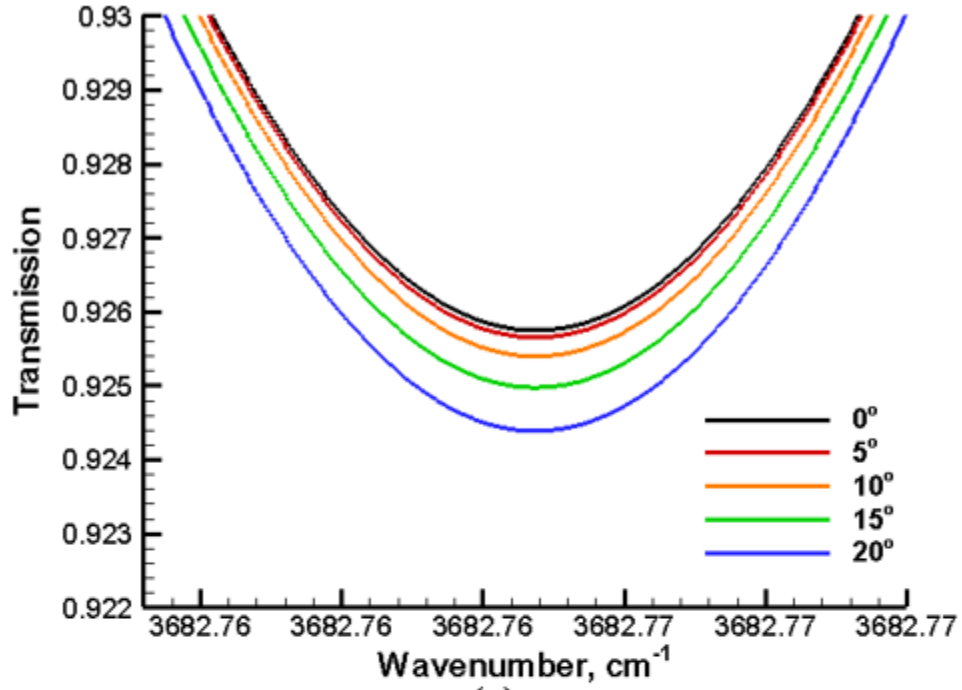
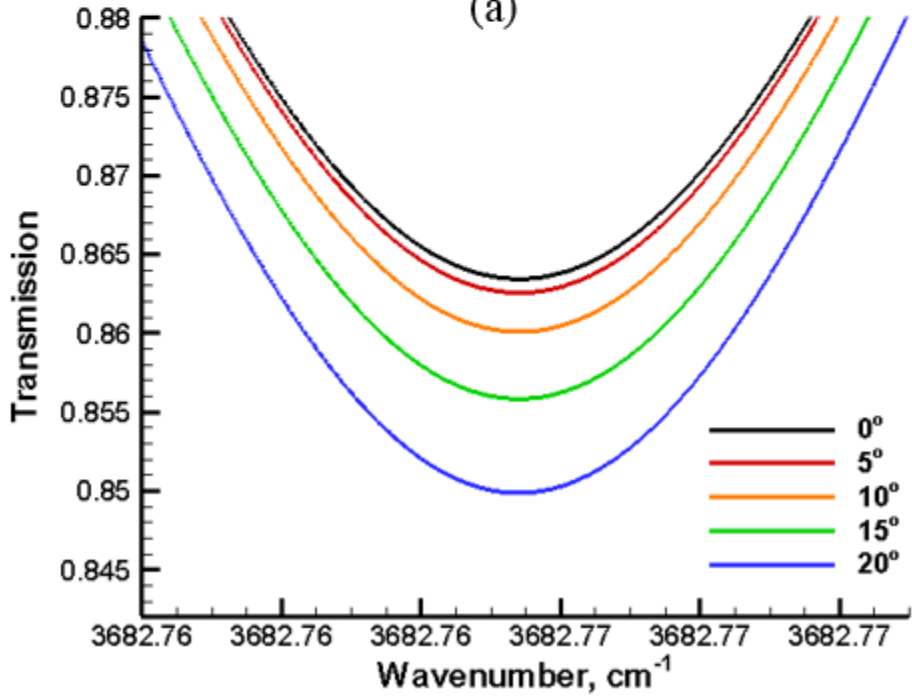


Fig. 18: Distance off cylinder surface comparisons for (a) non-catalytic cases and (b) super-catalytic cases.

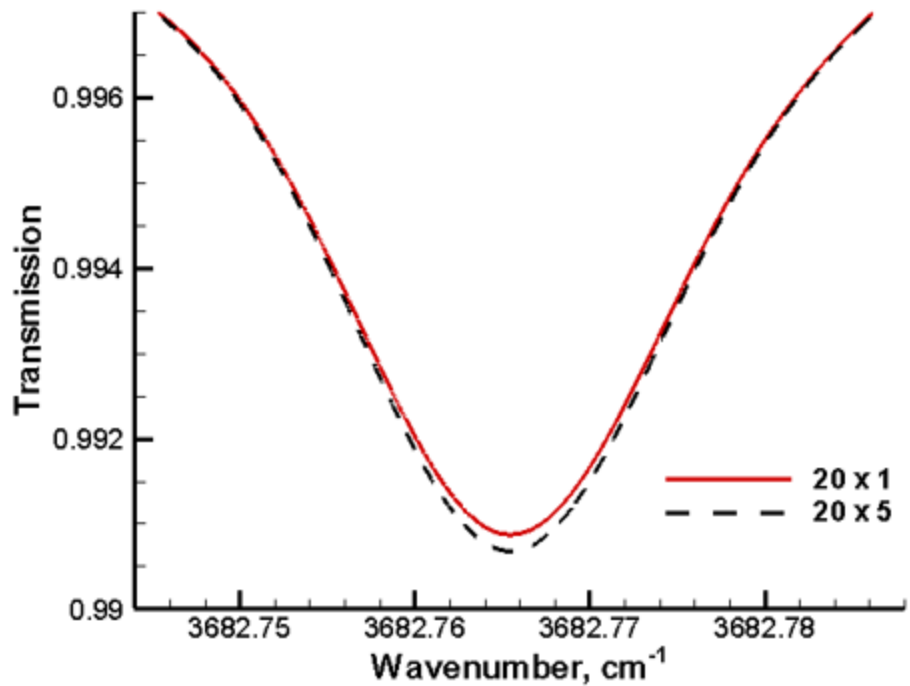


(a)

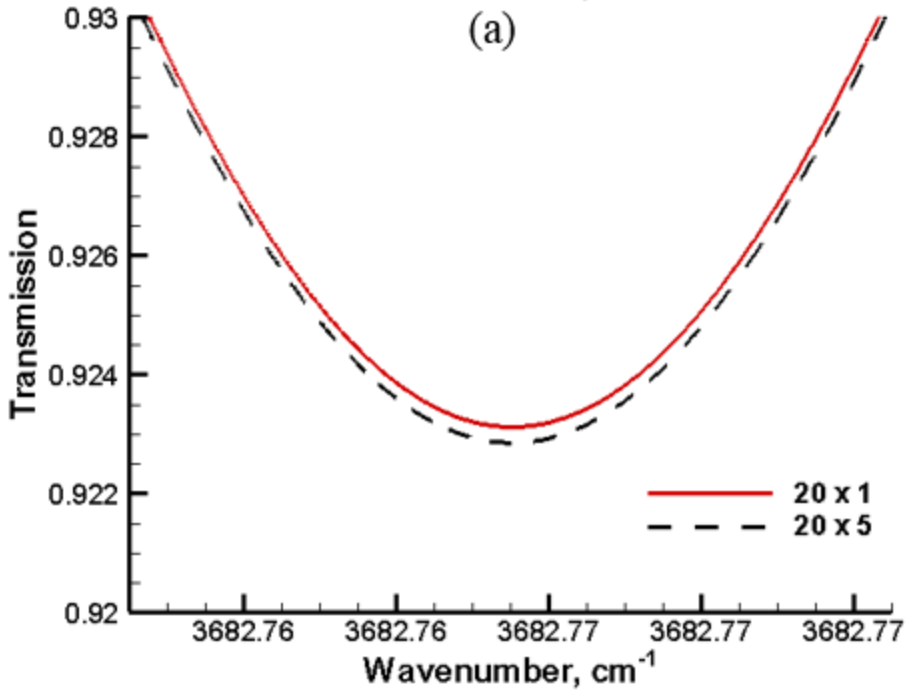


(b)

Fig. 19: Angle of pixel element off the stagnation line comparison for (a) non-catalytic cases and (b) super-catalytic cases.



(a)



(b)

Fig. 20: Transmission plots for full pixel simulation (20x5) and single line pixel simulation (20x1) for the (a) non-catalytic case and (b) super-catalytic cases.

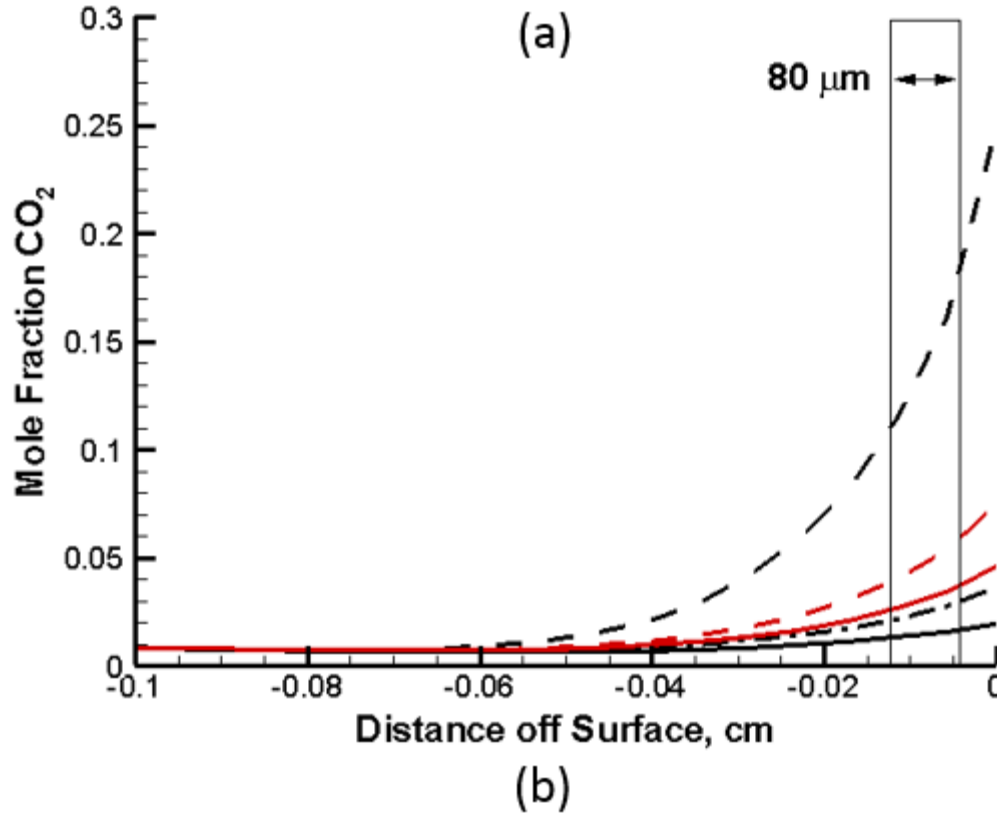
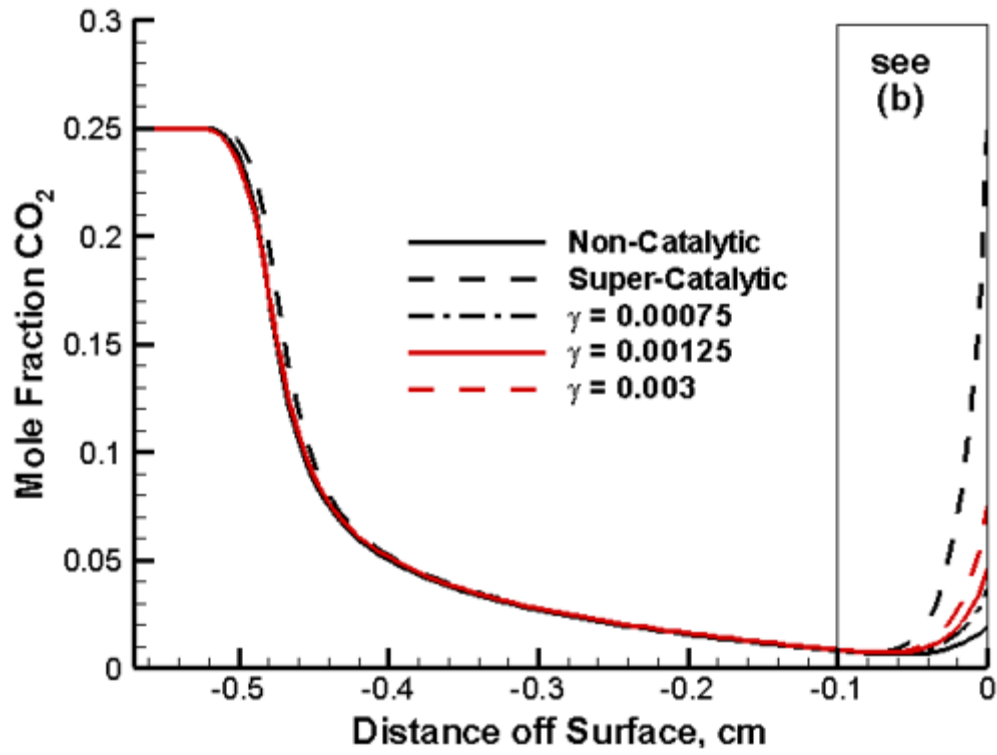


Fig. 21: Stagnation line mole fraction profiles in (a) the shock layer for various reaction efficiencies, with (b) zoom-in view of near-surface region.

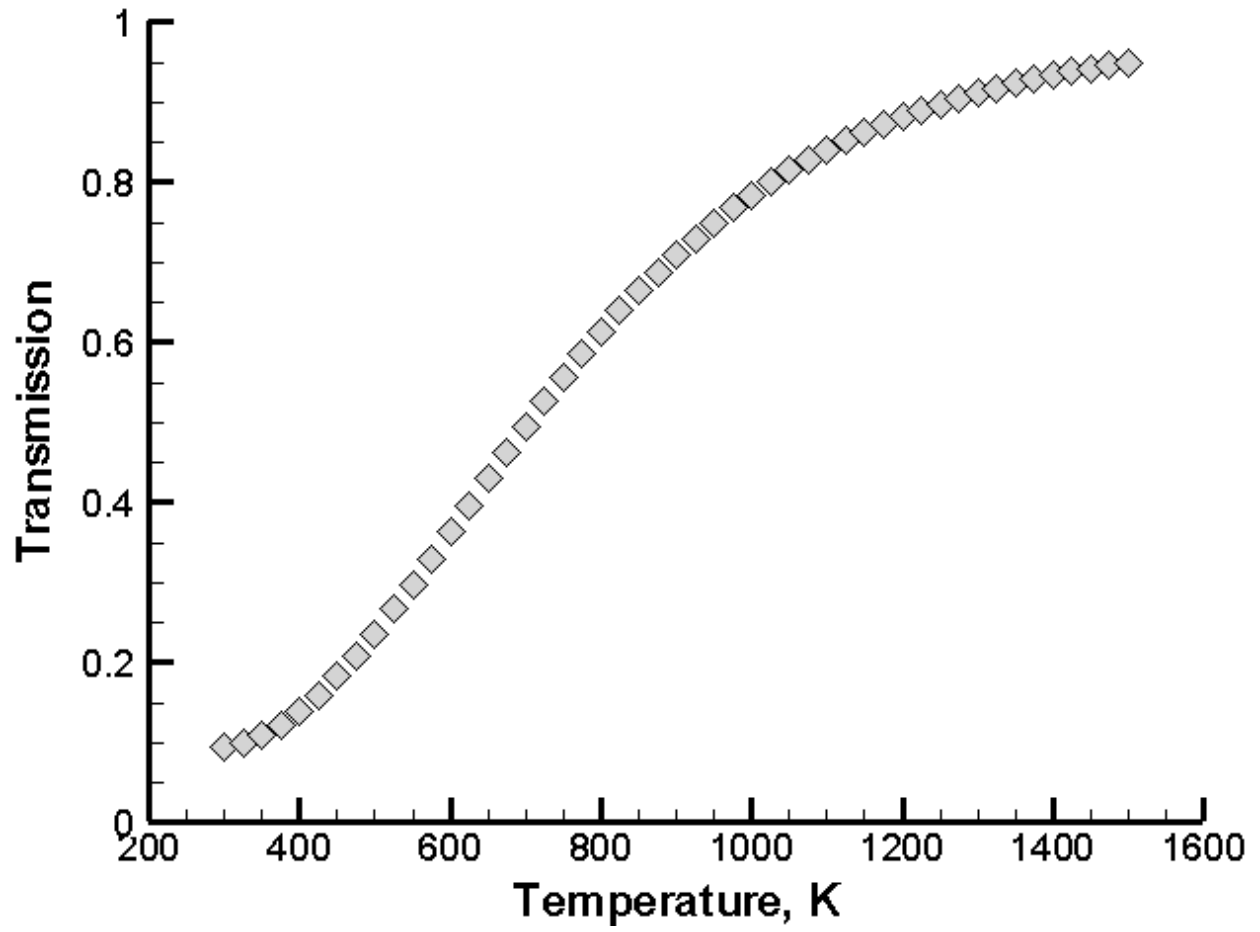


Fig. 22: Temperature dependence of CO₂ transition used in experiment.

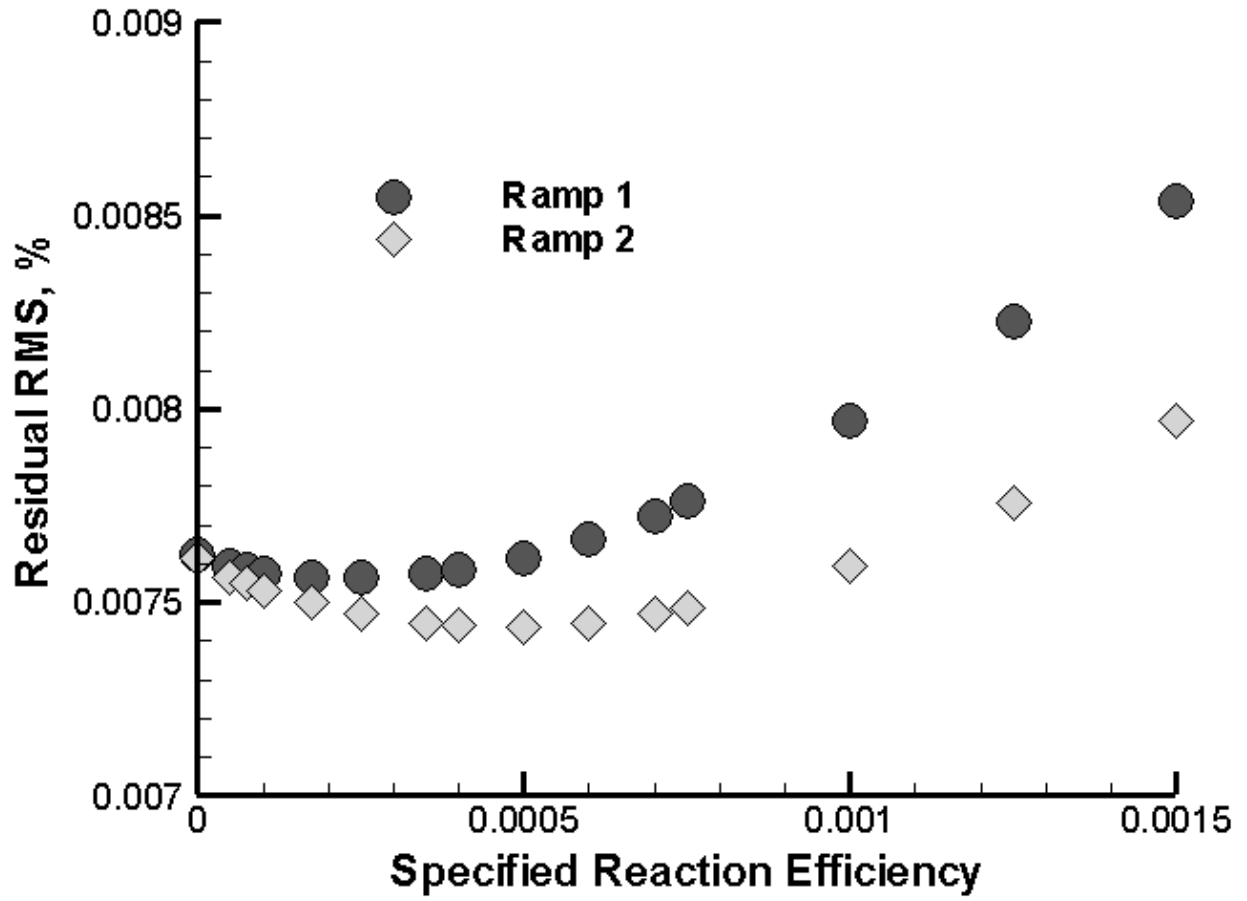


Fig. 23: RMS error of the residual between raw data and simulations for both ramps 1 and 2.

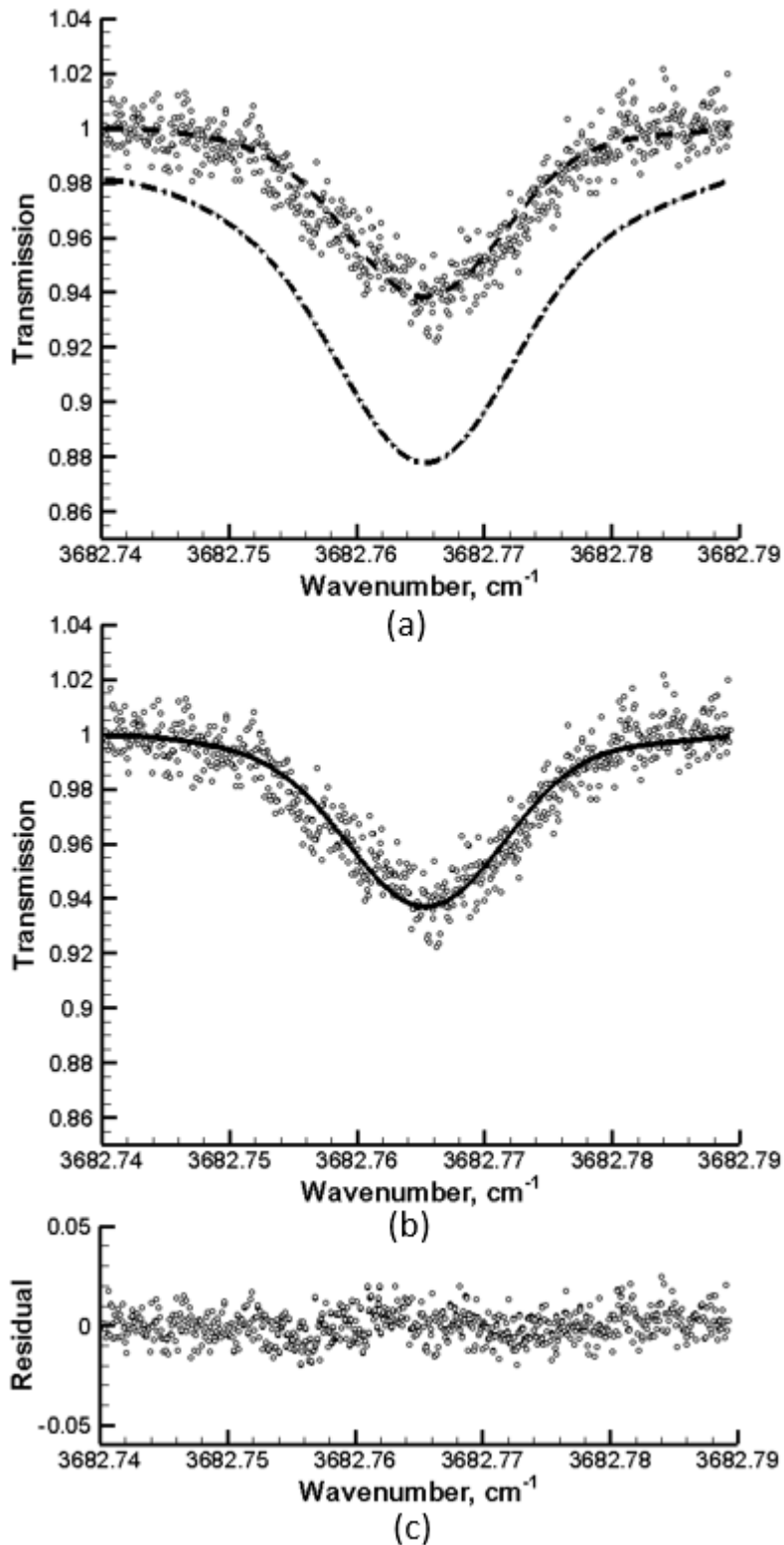


Fig. 24: Experimental results and simulations for non-catalytic, super-catalytic, and reaction efficiency $\gamma = 0.00025$ for ramp 1 shown in (a). A zoomed in view of the absorption feature is shown in (b), with the residual in (c) for $\gamma = 0.00025$.

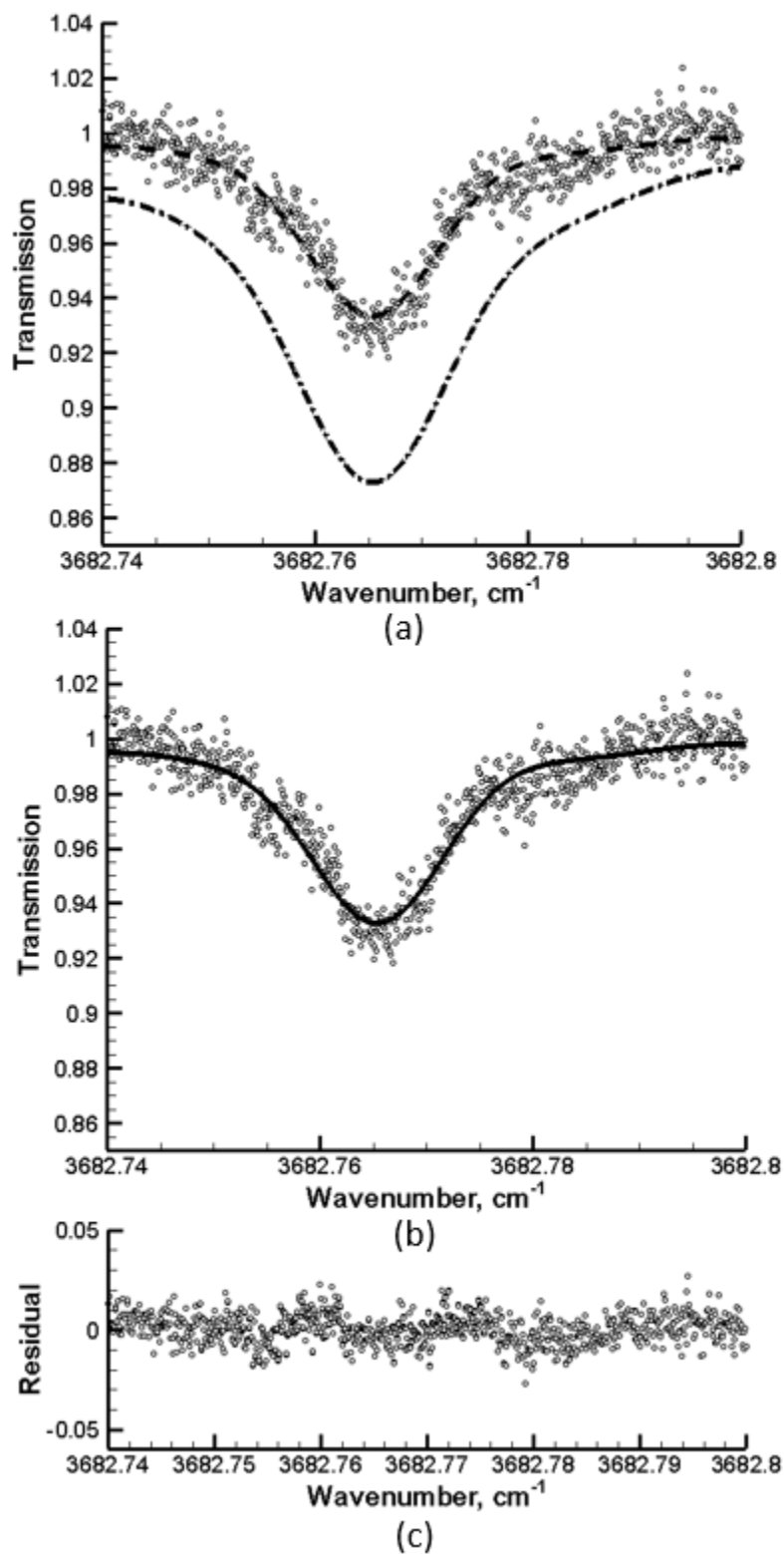


Fig. 25: Experimental results and simulations for non-catalytic, super-catalytic, and reaction efficiency $\gamma = 0.0005$ for ramp 2 shown in (a). A zoomed in view of the absorption feature is shown in (b), with the residual in (c) for $\gamma = 0.0005$.

5 Conclusions

An experimental setup using TDLAS was constructed to measure the concentration of CO₂ at the surface of a cylinder in order to describe the catalytic behavior of vehicles in hypersonic flows. Experimental data from the LENS-XX expansion tunnel was obtained for a 2 *inch* diameter, 2.5 *inch* long aluminum cylinder. The expansion tunnel has the benefit of an uncontaminated freestream gas composition, as opposed to reflected shock tunnels and arc jet facilities. The selected CO₂ absorption line is located at 2.7153 μm (3682.765 cm^{-1}), and was chosen such that interference from other molecules over the laser beam path length was negligible. The DPLR and CHEETAh CFD codes were used to obtain numerical results for various catalytic reaction efficiencies for use in simulating the transmission spectrum. A line-by-line absorption code based off the Beer-Lambert law was developed to use parameters obtained from the CFD simulations as inputs in order to simulate the transmission spectrum for comparison to experimental data. The raw data obtained in the experimental measurements was converted to transmission in wavenumber space for comparison to the simulations.

CFD solutions were obtained for cylinder flows in order to extract data along the cylinder surface and around the edges. The freestream flow profiles were obtained through a full facility DPLR simulation, coupled with results from CHEETAh. Sensitivity studies were carried out to investigate the effect of small perturbations in simulation parameters on the overall simulated transmission spectrum. Negligible perturbations include the detector element size, detector element angle above the stagnation line, expanding flow around the cylinder edges, and the number of lines used for the simulation of the pixel element. The detector element distance off the surface

of the cylinder was important to know accurately. The measured simulation detector element size was $80\ \mu\text{m}$, located $40\ \mu\text{m}$ off the cylinder surface, at an angle of five degrees above the stagnation line. Simulations from various CFD solutions were plotted with the experimental data. The non-catalytic and super-catalytic solutions bound the data. Simulations were performed using different values of the catalytic recombination efficiency, and the best-fit value is $\gamma_{\text{CO}} = 0.00025$ to 0.0005 for both data ramps within the test time. This efficiency significantly limits the maximum energy reclamation possible at the surface, indicating that TPS designs can avoid using the conservative super-catalytic wall boundary condition for the design process. These results are an important step towards understanding the catalytic nature of vehicles in hypersonic flows, and in validating aerothermal CFD codes with ground test facilities.

A major goal of this effort was to design the experimental setup, validate the measurement technique, and develop the post-processing and reconstruction process necessary to interpret the measured data. This objective has been successful, with the intent that this technique can also be used for the study of oxidizing carbon surfaces releasing carbon dioxide and carbon monoxide with the proper selection of higher temperature absorption lines.

Bibliography

- [1] MacLean, M., and Holden, M., "Catalytic Effects on Heat Transfer Measurements for Aerothermal Studies with CO₂," *44th AIAA Aerospace Sciences Meeting and Exhibit*, AIAA, Reno, NV, 2006.
- [2] MacLean, M., Marineau, E., Parker, R., Dufrene, A., Holden, M., and DesJardin, P., "Effect of Surface Catalysis on Measured Heat Transfer in Expansion Tunnel Facility," *Journal of Spacecraft and Rockets*, Vol. 50, No. 2, 2012, pp. 470-475.
- [3] MacLean, M., Wadhams, T., Holden, M., and Hollis, B., "Investigation of Blunt Bodies with CO₂ Test Gas Including Catalytic Effects," *38th AIAA Thermophysics Conference*, AIAA, Toronto, ON, 2005.
- [4] Zhou, X., Liu, X., Jeffries, J. B., and Hanson, R. K., "Development of a sensor for temperature and water concentration in combustion gases using a single tunable diode laser," *Measurement Science Technology*, Vol. 14, No. 8, 2003, pp. 1459.
- [5] Mohamed, A., Rosier, B., Henry, D., Louvet, Y., and Varghese, P. L., "Tunable diode laser measurements on nitric oxide in a hypersonic wind tunnel," *AIAA Journal*, Vol. 34, No. 3, 1996, pp. 494-499.
- [6] Parker, R., Wakeman, T., MacLean, M., and Holden, M., "Measuring Nitric Oxide Freestream Concentration Using Quantum Cascade Lasers at CUBRC," *44th AIAA Aerospace Sciences Meeting and Exhibit*, AIAA, Reno, NV, 2006.
- [7] Pekakovic, D.A., Marschall, J., Duan, L., and Martin, M. P., "Nitric Oxide Production from Surface Recombination of Oxygen and Nitrogen Atoms," *Journal of Thermophysics and Heat Transfer*, Vol. 22, No. 2, 2008, pp. 178-186.
- [8] Pejakovic, D.A., Marschall, J., Duan, L., and Martin, M. P., "Direct Detection of NO Produced by High-Temperature Surface-Catalyzed Atom Recombination," *Journal of Thermophysics and Heat Transfer*, Vol. 24, No. 3, 2010, pp. 603-611.
- [9] Weisberger, J., DesJardin, P., MacLean, M., and Parker, R., "Near-Surface Nitric Oxide Concentration Measurement in the LENS-XX Expansion Tunnel Facility," *44th AIAA Thermophysics Conference*, AIAA, San Diego, CA, 2013.
- [10] Gharavi, M., and Buckley, S. G., "Single diode laser sensor for wide-range H₂O temperature measurements," *Applied Spectroscopy*, Vol. 58, No. 4, 2004, pp. 468-73.

- [11] Barbu, T.L., Vinogradov, I., Durry, G., Korablev, O., Chassefière, E., and Bertaux, J. L., "TDLAS a laser diode sensor for the in situ monitoring of H₂O, CO₂ and their isotopes in the Martian atmosphere," *Advances in Space Research*, Vol. 38, No. 4, 2006, pp. 718-725.
- [12] Uddi, M., Das, A. K., and Sung, C., "Temperature measurements in a rapid compression machine using mid-infrared H₂O absorption spectroscopy near 7.6 μm ," *Applied Optics*, Vol. 51, No. 22, 2012, pp. 5464-5476.
- [13] Vanderover, J., and Oehlschlaeger, M. A., "A mid-infrared scanned-wavelength laser absorption sensor for carbon monoxide and temperature measurements from 900 to 4000 K," *Applied Physics B*, Vol. 99, No. 1-2, 2010, pp. 353-362.
- [14] Farooq, A., Jeffries, J. B., and Hanson, R. K., "CO₂ concentration and temperature sensor for combustion gases using diode-laser absorption near 2.7 μm ," *Applied Physics B*, Vol. 90, No. 3-4, 2008, pp. 619-628.
- [15] Meyers, J. M., and Fletcher, D., "Diode Laser Absorption Sensor Design and Qualification for CO₂ Hypersonic Flows," *Journal of Thermophysics and Heat Transfer*, Vol. 25, No. 2, 2011, pp. 193-200.
- [16] Pogány, A., Ott, O., Werhahn, O., and Ebert, V., "Towards traceability in CO₂ line strength measurements by TDLAS at 2.7 μm ," *Journal of Quantitative Spectroscopy and Radiative Transfer*, Vol. 130, No. 0, 2013, pp. 147-157.
- [17] Wu, K., Li, F., Cheng, X., Yang, Y., Lin, X., and Xia, Y., "Sensitive detection of CO₂ concentration and temperature for hot gases using quantum-cascade laser absorption spectroscopy near 4.2 μm ," *Applied Physics B*, Vol. 117, No. 2, 2014, pp. 659-666.
- [18] Vallon, R., Soutadé, J., Vérant, J., Meyers, J., Paris, S., and Mohamed, A., "A Compact Tunable Diode Laser Absorption Spectrometer to Monitor CO₂ at 2.7 μm Wavelength in Hypersonic Flows," *Sensors*, No. 6, pp. 6081-6091, 2010.
- [19] Dufrene, A., MacLean, M., Parker, R. A., Wadhams, T., and Holden, M., "Characterization of the New LENS Expansion Tunnel Facility," *48th AIAA Aerospace Sciences Meeting*, AIAA, Orlando, FL, 2010.
- [20] Dufrene, A., MacLean, M., Parker, R., and Holden, M., "Experimental Characterization of the LENS Expansion Tunnel Facility Including Blunt Body Surface Heating," *49th AIAA Aerospace Sciences Meeting*, AIAA, Orlando, FL, 2011.
- [21] Zhou, X., Jeffries, J. B., and Hanson, R. K., "Development of a fast temperature sensor for combustion gases using a single tunable diode laser," *Applied Physics B*, Vol. 81, No. 5, 2005, pp. 711-722.
- [22] Wright, M. J., Candler, G. V., and Bose, D., "Data-Parallel Line Relaxation Method for the Navier-Stokes Equations," *AIAA Journal*, Vol. 39, No. 9, 1998, pp. 1603-1609.

- [23] MacCormack, R. W., and Candler, G. V., "The solution of the Navier-Stokes equations using Gauss-Seidel line relaxation," *Computers & Fluids*, Vol. 17, No. 1, 1989, pp. 135-150.
- [24] Palmer, G. E., and Wright, M. J., "A Comparison of Methods to Compute High-Temperature Gas Viscosity," *8th AIAA/ASME Joint Thermophysics and Heat Transfer Conference*, AIAA, St. Louis, MO, 2002.
- [25] Palmer, G. E., and Wright, M. J., "A Comparison of Methods to Compute High-Temperature Gas Thermal Conductivity," *36th AIAA Thermophysics Conference*, AIAA, Orlando, FL, 2003.
- [26] Gupta, R. N., Yos, J. M., Thompson, R. A., and Lee, K. P., "A Review of Reaction Rates and Thermodynamic and Transport Properties for an 11-Species Air Model for Chemical and Thermal Nonequilibrium Calculations to 30,000 K," NASA RP-1232. August 1990.
- [27] Wright, M. J., Bose, D., Palmer, G. E., and Levin, E., "Recommended Collision Integrals for Transport Property Computations, Part 1: Air Species," *AIAA Journal*, Vol. 43, No. 12, 2005, pp. 2558-2564.
- [28] Wright, M. J., Hwang, H. H., and Schwenke, D. W., "Recommended Collision Integrals for Transport Property Computations Part 2: Mars and Venus Entries," *AIAA Journal*, Vol. 45, No. 1, 2007, pp. 281-288.
- [29] Ramshaw, J. D., "Self-Consistent Effective Binary Diffusion in Multicomponent Gas Mixtures," *Journal of Non-Equilibrium Thermodynamics*, Vol. 15, No. 3, 1990, pp. 295-300.
- [30] Park, C., Howe, J. T., Jaffe, R. L., and Candler, G. V., "Review of Chemical-Kinetic Problems of Future NASA Missions, II: Mars Entries," *Journal of Thermophysics and Heat Transfer*, Vol. 8, No. 1, 1994, pp. 9-23.
- [31] Candler, G. V., "Chemistry of External Flows," *Aerothermochemistry for Hypersonic Technology: Von Karman Institute for Fluid Dynamics Lecture Series*, VKI LS 1995-04.
- [32] Landau, L., and Teller, E., "Theory of Sound Dispersion," *Physikalische Zeitschrift der Sowjetunion*, Vol. 10, No. 34, 1936.
- [33] Millikan, R. C., and White, D. R., "Systematics of Vibrational Relaxation," *Journal of Chemical Physics*, Vol. 39, No. 12, 1963, pp. 3209-3213.
- [34] Camac, M., "CO₂ Relaxation Processes in Shock Waves," *Fundamental Phenomena in Hypersonic Flow*, J.G. Hall Ed. Cornell University Press, 1964, pp. 195-215.

- [35] Park, C., “Assessment of Two-temperature Kinetic Model for Ionizing Air.” *Journal of Thermophysics and Heat Transfer*, Vol. 3, No. 3, 1989, pp. 233-244.
- [36] Marschall, J., and MacLean, M., “Finite-Rate Surface Chemistry Model, I: Formulation and Reaction System Examples,” *42nd AIAA Thermophysics Conference*, AIAA, Honolulu, HI, 2011.
- [37] MacLean, M., Marschall, J., and Driver, D. M., “Finite-Rate Surface Chemistry Model, II: Coupling to Viscous Navier-Stokes Code,” *42nd AIAA Thermophysics Conference*, AIAA, Honolulu, HI, 2011.
- [38] Bose, D., Wright, M. J., and Palmer, G. E., “Uncertainty Analysis of Laminar Aeroheating Predictions for Mars Entries,” *Journal of Thermophysics and Heat Transfer*, Vol. 20, No. 4, 2006, pp. 652 – 662.
- [39] Sepka, S., Chen, Y. K., Marschall, J., and Copeland, R. A., “Experimental Investigation of Surface Reactions in Carbon Monoxide and Oxygen Mixtures,” *Journal of Thermophysics and Heat Transfer*, Vol. 14, No. 1, 2000, pp. 45-52.
- [40] Steinfeld, J. I., Francisco, J. S., Has, W. L., “Chemical Kinetics and Dynamics”, 2nd Edition, Prentice Hall, 1999.
- [41] Wright, M. J., Olejniczak, J., Brown, J. L., Hornung, H. G., and Edquist, K. T., “Modeling of Shock Tunnel Aeroheating Data on the Mars Science Laboratory Aeroshell,” *Journal of Thermophysics and Heat Transfer*, Vol. 20, No. 4, 2006, pp. 641 – 651.
- [42] Rothman, L. S., Gordon, I. E., Barbe, A., Benner, D. Chris, Bernath, P. F., Birk, M., et al., “The HITRAN 2008 Molecular Spectroscopic Database,” *JQSRT*, 110, pp. 533-572, 2009.
- [43] McLean, A. B., Mitchell, C. E. J., and Swanston, D. M., “Implementation of an efficient analytical approximation to the Voigt function for photoemission lineshape analysis,” *In-house report*, Department of Physics, Queen’s University, Kingston, Ontario, 2002.
- [44] MacLean, M., Dufrene, A., and Holden, M., “Spherical Capsule Heating in High Enthalpy Carbon Dioxide in LENS-XX Expansion Tunnel,” *51st AIAA Aerospace Sciences Meeting including the New Horizons Forum and Aerospace Exposition*, AIAA, Grapevine, TX, 2013.